LIVERPOOL JOHN MOORES UNIVERSITY

LJMU Research Online

Rathborne, JM, Whitaker, JS, Jackson, JM, Foster, JB, Contreras, Y, Stephens, IW, Guzman, AE, Longmore, SN, Sanhueza, P, Schuller, F, Wyrowski, F and Urquhart, JS

Molecular Line Emission Towards High-Mass Clumps: The MALT90 Catalogue

http://researchonline.ljmu.ac.uk/id/eprint/4139/

Article

Citation (please note it is advisable to refer to the publisher's version if you intend to cite from this work)

Rathborne, JM, Whitaker, JS, Jackson, JM, Foster, JB, Contreras, Y, Stephens, IW, Guzman, AE, Longmore, SN, Sanhueza, P, Schuller, F, Wyrowski, F and Urquhart, JS (2016) Molecular Line Emission Towards High-Mass Clumps: The MALT90 Catalogue. PUBLICATIONS OF THE

LJMU has developed **LJMU Research Online** for users to access the research output of the University more effectively. Copyright © and Moral Rights for the papers on this site are retained by the individual authors and/or other copyright owners. Users may download and/or print one copy of any article(s) in LJMU Research Online to facilitate their private study or for non-commercial research. You may not engage in further distribution of the material or use it for any profit-making activities or any commercial gain.

The version presented here may differ from the published version or from the version of the record. Please see the repository URL above for details on accessing the published version and note that access may require a subscription.

For more information please contact researchonline@ljmu.ac.uk

http://researchonline.ljmu.ac.uk/

Publications of the Astronomical Society of Australia (PASA)
© Astronomical Society of Australia 2016; published by Cambridge University Press.
doi: 10.1017/pas.2016.xxx.

Molecular line emission toward high-mass clumps: the MALT90 catalog

J. M. Rathborne[1], J. S. Whitaker[2], J. M. Jackson[3], J. B. Foster[4], Y. Contreras[1], I. W. Stephens[3] , A. E. Guzmán[5], S. N. Longmore[6], P. Sanhueza[7], F. Schuller[8], F. Wyrowski[9], and J. Urquhart[9]
[1]CSIRO Astronomy and Space Science, PO Box 76, Epping, NSW 1710, Australia
[2]Physics Department, Boston University, Boston, MA 02215, USA
[3]Institute for Astrophysical Research, Boston University, Boston, MA 02215, USA
[4]Department of Astronomy, Yale University, P.O. Box 208101 New Haven, CT 06520-8101, USA
[5]Departamento de Astronomía, Universidad de Chile, Camino el Observatorio 1515, Las Condes, Santiago, Chile
[6]Astrophysics Research Institute, Liverpool John Moores University, 146 Brownlow Hill, Liverpool L3 5RF, UK
[7]National Astronomical Observatory of Japan, 2-21-1- Osawa, Mitaka, Tokyo 181-8588, Japan
[8]European Southern Observatory, Alonso de Cordova 3107, Vitacura, Santiago, Chile
[9]Max Planck Institute for Radioastronomy, Auf dem Hugel 69, 53121, Bonn, Germany

Abstract
The Millimetre Astronomy Legacy Team 90 GHz (MALT90) survey aims to characterise the physical and chemical evolution of high-mass clumps. Recently completed, it mapped 90 GHz line emission toward 3246 high-mass clumps identified from the ATLASGAL 870 μm Galactic plane survey. By utilising the broad frequency coverage of the Mopra telescope's spectrometer, maps in 16 different emission lines were simultaneously obtained. Here we describe the first line catalog of the detected emission, generated by Gaussian profile fitting to spectra extracted toward each clumps' dust peak. Synthetic spectra show that the catalog has a completeness of >95%, a probability of a false-positive detection of <0.3%, and a relative uncertainty in the measured quantities of <20% over the range of detection criteria. We find that the detection rates are highest for the (1–0) molecular transitions of HCO^+, HNC, N_2H^+, and HCN (72–88%). The majority of clumps ($\sim$ 95%) are detected in at least one of the molecular transitions, just under half of the clumps ($\sim$ 48%) are detected in 4 or more of the transitions, while only 2 clumps are detected in 13 or more transitions. We find several striking trends in the ensemble of properties for the different molecular transitions when plotted as a function of the clumps' evolutionary state. In particular, the optically thickest HCO^+ emission shows a 'blue-red asymmetry' that indicates overall collapse that monotonically decreases as the clumps evolve. This catalog represents the largest compiled database of molecular line emission toward high-mass clumps and is a valuable data set for detailed studies of these objects.

Keywords: interstellar medium – molecular clouds – star formation

1 INTRODUCTION

High-mass stars (>8 $M_\odot$) typically form in clusters from dense molecular clumps with sizes of $\sim$ 1 pc and masses of $\gtrsim$ 200 $M_\odot$. Recent infrared and millimetre/submillimetre Galactic plane surveys have identified a large number of dense molecular clumps in all stages of evolution (e.g., Benjamin et al. 2003; Churchwell et al. 2009; Carey et al. 2009; Molinari et al. 2010; Schuller et al. 2009; Aguirre et al. 2011). In order to better understand the environment within which high-mass stars and clusters form, we must characterise the global conditions within, and evolution of, the high-mass clumps from which they form.

The Millimetre Astronomy Legacy Team 90 GHz (MALT90) survey aims to achieve this by determining the physical and chemical evolution within $\sim$ 3000 high-mass clumps located throughout the Galaxy (Foster et al. 2011; Jackson et al. 2013; Foster et al. 2013). In doing so, it provides a legacy database for the study of high-mass star formation.

Over four Austral winter semesters (2010–2013) using the 22-m Mopra telescope, MALT90 obtained 3' × 3' maps toward 2012 locations along the Galactic plane[1]. Jackson et al. (2013) provides the full details of the survey strategy, observing procedure, and data reduction. The map locations were selected to cover dense clumps

[1]All raw data and processed cubes and moment maps for the clumps observed as part of MALT90 are publicly available through the Australia Telescope Online Archive (ATOA; http://atoa.atnf.csiro.au/).

identified within the ATLASGAL 870 μm dust continuum emission survey (Schuller et al. 2009)

Schuller et al. (2009) estimate that, for cold dust with T_{dust} = 10 K, the ATLASGAL 870 μm peak flux sensitivity of 0.25 Jy corresponds to a clump mass of 200 $M_\odot$ at a distance of 10 kpc. MALT90 used this flux sensitivity to select clumps from the ATLASGAL catalogs of Contreras et al. (2013) and Urquhart et al. (2014). In addition to this flux sensitivity limit, we further imposed criteria based on the clumps' level of IR emission (to ensure that clumps in all stages of star formation activity were included within the survey) and gave preference to those located in the Galaxy's 4th quadrant.

By utilising the broad frequency coverage of the Mopra telescope's spectrometer, maps in 16 different emission lines near 90 GHz were obtained simultaneously. The transitions covered by the MALT90 survey (see Table 1 for details) were selected to be unambiguous probes of the dense clumps, located within larger, more diffuse giant molecular clouds (GMCs), that will give rise to stars. Because the 90 GHz molecules require high volume densities for their excitation (10^5–10^6 cm^{-3}) and span a range in their excitation energies (5–50 K; Müller et al. 2001, 2005; Schöier et al. 2005), they are excellent tracers of distinct physical conditions. Moreover, they also probe distinct stages of chemical evolution: the chemistry evolves quite substantially from the cold gas phase to the hot gas phase around a newly formed high-mass star. As such, the presence or absence of emission from these molecules can also indicate distinct stages of chemical evolution.

Now complete, MALT90 is the largest database of molecular line emission toward high-mass clumps. Because the maps have good spatial (38") and excellent spectral (0.11 km s^{-1}) resolution, they reveal a wealth of information about the clump morphologies, chemistry, and kinematics. The survey can be utilised to both characterise the ensemble properties and evolution of high-mass clumps and to identify outliers within the population. Indeed, several studies have already begun to utilise the survey for these purposes (e.g., Hoq et al. 2013; Liu et al. 2013; Miettinen 2014; Rathborne et al. 2014a; He et al. 2015; Stephens et al. 2015; Yu & Wang 2015). In addition, MALT90 also provides a definitive source list for detailed ALMA observations aimed at understanding the evolution of a high-mass clump. Indeed, ALMA cycle 0 observations toward a high-mass MALT90 clump, G0.253+0.016, shows remarkable structure on small spatial scales (Rathborne et al. 2014b, 2015) and reveals details about mass assembly before star formation has begun.

Here we report the properties of the molecular line emission detected toward the 870 μm dust continuum peak of each clump observed as part of the MALT90 survey determined via Gaussian profile fitting to the spectra. Figures 1 – 8 provide an overview of the ATLASGAL/*Spitzer* images and MALT90 spectra toward selected clumps contained within the catalog. These figures are included to show examples of the Gaussian profile fitting procedures and reported catalog values that are described in the following sections. We discuss these in more detail in section 5.

2 CHARACTERISING THE STAR-FORMATION ACTIVITY WITHIN EACH CLUMP

To ascertain the star formation activity within each clump, *Spitzer* images (3–24 μm) were used to classify each into five broad categories: 'quiescent' clumps (these are IR dark and trace cold and dense dust), 'protostellar' clumps (these have either extended 4.5 μm emission or a compact 24 μm point source indicating shocked gas or an embedded, accreting protostar), 'H II regions' (these are IR bright and either compact or extended), and 'PDRs' (Photo-dominated regions; these occur at the molecular/ionised gas interface and are excited by the UV radiation from a nearby high-mass star).

We also use an additional category (referred to as 'uncertain') to separate out clumps for which there are no obvious IR signatures, either dark or bright, associated with them. Since the dust emission from ATLASGAL traces material along the line of sight across the Galaxy but *Spitzer* is sensitive to nearby emission only, many of these 'uncertain' clumps may in-fact lie at the far side of the Galaxy. For simplicity and to ensure that these IR-based categories contain only clumps for which IR signatures (either dark or bright) are clearly associated, we exclude the 'uncertain' clumps from any analysis that is based on these IR categories.

Within the survey we classify 688 clumps as 'quiescent' ('Q'), 794 as 'protostellar', ('A'), 189 as compact H II regions ('C'), 747 as extended 'H II regions' ('H'), 362 as 'PDRs' ('P'), and 777 as 'uncertain' ('U'). Since these IR-based categories broadly represent the stages in evolution for a clump with increasing levels of active star-formation, we use these categories as a proxy for evolution: quiescent clumps represent an early phase, protostellar clumps show the initial signatures of active star formation, while H II regions represent a later stage when young, high-mass stars have already formed.

3 CHARACTERISING THE LINE EMISSION TOWARD EACH CLUMP

Mapping around each of the ATLASGAL clumps was required in order to address many of the science goals of the MALT90 survey. These maps reveal that the spatial distribution of emission from the various gas tracers within a clump can often be very different (see e.g., Jackson et al. 2013; Hoq et al. 2013; Stephens et al. 2015). In order to generate a manageable summary of

the line emission detected within MALT90, we choose to first catalog the properties of the line emission toward the dust peak of each of the ATLASGAL clumps. This first catalog will, therefore, not include information on the spatial distribution, velocity field, or line profile variations across the clumps that the maps do provide. Nevertheless, this catalog provides a summary of the emission detected toward the 870 μm dust continuum peak of each clump and an easy searchable list from which to select clumps for more detailed analyses.

3.1 Spectra toward each high-mass clump

For each clump we have extracted an averaged spectrum from the MALT90 datacubes for each of the 16 emission lines. The spectra were created by averaging the spectra in a 3×3 pixel ($27'' \times 27''$) box around the clump's dust peak determined from the ATLASGAL catalogs. The size of the averaging box was selected to maximise the signal to noise of the fainter emission and is approximately the angular resolution of MALT90 (for details on the data reduction pipeline, see Jackson et al. 2013). Note, all spectra and Gaussian profile fitting are shown and performed on the T_A^* scale. To convert to main-beam brightness temperature (T_{mb}), divide the antenna temperature (T_A^*) by the main-beam efficiency (η_{mb}) of 0.49 (Ladd et al. 2005).

Because some MALT90 maps covered more than one ATLASGAL clump, the total number of clumps that we have spectra for (3246) is greater than the number of maps obtained (2012).

3.2 Additional baseline subtraction

While a first order baseline subtraction was performed during the automated processing of the data cubes (see Jackson et al. 2013) we found that the reliability of the Gaussian profile fitting was often considerably improved when we performed an additional higher-order fit to the baseline. This was necessary because in poorer weather the MALT90 spectra were often contaminated by non-linear baselines and baseline ripple, especially at the highest frequency band containing N_2H^+. Consequently, a first order polynomial was often an inadequate model of the baseline, and the automated routine often failed to properly select signal-free velocity ranges. This additional baseline fit and subtraction was individually performed on each spectrum.

3.3 Noise estimation

The root-mean-square (rms) noise level in each spectrum was calculated from a comparison of the amplitude for each odd-numbered channel with the amplitude in the preceding even-numbered channel via

$$\sigma_{noise} = 1.067\sqrt{\frac{\langle (y_{2j+1} - y_{2j})^2 \rangle_j}{2}},$$

where y_j is the amplitude in channel j. This assumes Gaussian noise in the presence of a slowly-varying spectral signal or baseline variations much broader than the spectral channel spacing. This channel-to-channel estimator of σ_{noise} is robust against the presence of baseline ripples and line emission signals within the spectrum. As such, it represents a more accurate method to reliably determine, in an automated way, the noise level in a spectrum that may have baseline ripples and/or bright line emission anywhere within it, compared to common methods that first require the line to be identified and masked before then applying a simple standard deviation approach. The factor 1.067 corrects for the slight channel-to-channel correlation introduced by the subtraction of a smoothed reference spectrum in the MALT90 data reduction pipeline, the size of this correlation depends on the size of the smoothing window (the pipeline utilised Hanning smoothing with an 11-channel window, see Jackson et al. 2013).

Figure 9 shows the normalized cumulative distribution of σ_{noise} derived from the spectra of each emission line. The bold line shows the cumulative distribution for the synthetic spectra (see Section 3.5). The tail at high noise levels arises from spectra near the map edges and those obtained when the weather was variable. The derived noise distribution from the 16 emission lines follow each other closely, with the exception of HNCO 4(1,3)–3(1,2) which suffered from serious noise spikes and/or band distortions (shown with the dashed line). We examined all possible 'detections' of HNCO 4(1,3)–3(1,2) and concluded that there were no credible signals in any of the spectra; the detection flag in the catalog is always set to 'N' for this emission (see Section 2.4.3). For all other emission lines, 90% of the spectra have $\sigma_{noise} < 0.24$ K, while 50% have $\sigma_{noise} < 0.18$ K on the antenna temperature (T_A^*) scale.

3.4 Gaussian profile fitting

In order to characterise the detected emission toward each clump, we have fit each spectrum with either a single or multiple Gaussian profile(s). These profile fits provide key parameters typically used to describe line emission: peak antenna temperature (T_A^*), velocity width (ΔV), and central velocity (V_{LSR}). In the catalog we report the integrated intensity (II) calculated directly from summing the emission over the fit range, i.e., $II = \int T_A^* dv$, where dv is the spectra resolution. We choose to calculate II by summing the actuall emission, rather than using the derived Gaussian parameters, since the former will also include any component of the line that is non-Gaussian. The inte-

grated intensity signal-to-noise ratio, II_{SNR}, was determined by dividing the integrated intensity by σ_{II}, where $\sigma_{II} = \sqrt{N_{channel}}\sigma_{noise}dv$, and $N_{channel}$ is the number of channels in the fitting region. The antenna temperature signal-to-noise ratio, T_{SNR}, was defined as $T_{SNR} = T_A^* / \sigma_{noise}$.

The profile fitting was performed on the baseline-subtracted spectra as a two-step process: the first iteration was performed on the most prominent peaks in the HCO^+, HNC, and N_2H^+ spectra to determine a 'consensus' velocity (V_C), while the second iteration was performed on all 16 lines restricting the velocity range over which to search for emission to be $V_C \pm 5\,km\,s^{-1}$. This two-step method was employed as it resulted in significantly higher detection rates and more reliable fits to the fainter emission.

3.4.1 Determining a consensus velocity

For each clump, we determine a single 'consensus' velocity (V_C) to describe its associated line emission. Given that the transitions covered by the MALT90 survey probe different physical and chemical conditions, there may be slight differences in the derived V_{LSR} and specific kinematic signatures only evident from certain species (e.g., shocks and outflows from SiO and HCO^+). While these differences are informative, to simplify and summarise the derived velocities from the ensemble of molecular transitions, we determine and report a single 'consensus' velocity which is an estimator of the systemic velocity of the clump. Determining a single consensus velocity for each clump is important, since it will be used to derive the clump's kinematic distance (Whitaker et al. in prep.) and in combination with the dust continuum emission (Guzmán et al. 2015), their masses and luminosities (Contreras et al. in prep.).

To derive a consensus velocity for the clumps, we first focus on fitting to the most commonly detected and brightest emission lines covered by the survey: HCO^+, HNC, and N_2H^+. In determining the consensus velocity, we excluded velocity information from the bright HCN transition because the combination of high optical depths, hyperfine structure, and deep self-absorption often seen in this line resulted in complicated, non-Gaussian profiles, which led to unreliable velocities.

For each clump, emission peaks within the HCO^+, HNC, and N_2H^+ spectra were identified by finding the channel with the highest intensity. A profile was then fit to the spectrum around this channel. For HCO^+ and HNC the profile was a single Gaussian; for N_2H^+ the profile was a triple Gaussian constrained in velocity using the known hyperfine velocity offsets and a single line-width. If the fit produced a 'reliable' detection (i.e., with an $II_{SNR} > 4$ and $T_{SNR} > 1$) then the velocity and T_A^* for this profile were recorded, and the profile was subtracted from the spectrum. A second profile was then fit to the next brightest peak in the spectrum and was recorded if it too was a reliable detection. This resulted in, at most, 6 velocities: two distinct velocity components for the HNC, HCO^+, and N_2H^+.

The velocities were sorted by increasing value and aggregated in a single pass: starting from the lowest velocity, if the next higher velocity was within $5\,km\,s^{-1}$ then the two velocities were averaged, weighted by their amplitudes. After this procedure, the component with the greatest accumulated weight was identified as the first velocity component. If more than one velocity component survived the averaging procedure (i.e., their separation in velocity was $> 5\,km\,s^{-1}$), the component with the next highest weight was designated as the second velocity component.

For spectra where no second component was identified, we report in the catalog a single velocity component toward that dust peak and append an 'S' to the clump's name. In cases where two velocity components where identified and their velocities were within $15\,km\,s^{-1}$ of each other, we consider the emission to arise from the same physical clump ($15\,km\,s^{-1}$ was used to separate velocity components since this was three times the typically derived value for the line-width). We report a single velocity component toward that dust peak (clump name in the catalog is appended with an 'S') but indicate this decision by setting the number of Gaussians flag, 'NG', in the catalog to 2 (i.e., two Gaussian profiles were combined). In these cases, we report in the catalog values for T_A^*, V_{LSR} and ΔV (and their uncertainties) derived from a moment (intensity weighted) calculation of the combined line profile.

If the velocities from the two components were $> 15\,km\,s^{-1}$ apart, we consider the emission to arise from physically separate clumps along the line of sight and thus report two velocity components toward that dust peak (clump names in the catalog are appended with an 'A' and 'B'). In these cases, the first velocity component with the greatest sum in T_A^* derived from the three lines is reported as component 'A', the second velocity component is reported as component 'B'.

A consensus velocity was determined for ∼94% of our clumps; typically all three lines (HNC, HCO^+, and N_2H^+) were detected, and their velocities agreed within $< 1\,km\,s^{-1}$. A second velocity component was identified in 19% of the spectra; in 78% of these cases the additional velocity component appeared in only a single molecular line.

3.4.2 Fits to individual spectra

Once the consensus velocity for each clump was determined, a Gaussian profile was then fit to all 16 spectra by setting the search region to be $V_C \pm 5\,km\,s^{-1}$. If a consensus velocity was not found (i.e., there was no significant emission from HCO^+, HNC, or N_2H^+) then the search region was left unconstrained in velocity.

To increase the reliability of finding emission from the fainter lines at the same velocity as the brighter lines, the velocity range over which the fitting was performed was also restricted. The fitting range was determined individually for each spectrum: its centre was defined using the channel of the peak intensity found within the search region. The fitting range was then expanded in both positive and negative velocity directions until the first negative channel was found (i.e., the noise level was reached). As an extra buffer and to ensure that the fitting range was both wide enough to cover the emission and to include a sufficient number of channels to accurately describe the baseline, the fitting range was then increased by an additional 25 channels in both the positive and negative velocity directions (2.75 km s^{-1}) to establish the final fitting range.

Gaussian profiles were then fit to the spectrum within the fitting range. For the brightest velocity component (either 'S' or 'A') the first fit performed was that using a single Gaussian profile. A second fit was then performed using multiple Gaussian profiles. For molecules showing hyperfine splitting (C_2H, HCN, and N_2H^+) the second fit used multiple Gaussian components (either 2, 3 or 3 respectively) constrained in velocity using the known hyperfine velocity offsets for each molecule, a single line-width, but unconstrained amplitudes. For all other molecules, the second fit was performed using 2 unconstrained Gaussian profiles.

When a second velocity component was evident in the spectra (i.e., for components 'B'), we only perform a fit using a single Gaussian profile. The fitting for these components was simplified as they were often faint and rarely showed a profile that was not well fit by a simple, single Gaussian profile.

3.4.3 Selecting the best fit

For each fit, a χ^2 minimization was performed to determine the best-fit parameters, their uncertainties and a fit probability (T_A^*, ΔV, V_{LSR}, II, and P_{fit}). The fit probability is the integral of the normalised χ^2/DoF distribution above the value determined by the fit (where DoF represents the number of fit degrees of freedom). It therefore represents the probability that in an ensemble of well-modelled observations a value of χ^2/DoF greater than the observed value would arise due to statistical fluctuations. We found that the distributions of fit probabilities were reasonably flat, as expected if the Gaussian profile is appropriate to the line shape and the noise is accurately represented. A spike in the distribution at very small fit probability indicates cases where the fit was a poor representation of the data and its uncertainties.

We compared the probabilities of the two fits (either the single Gaussian profile fit or the multiple Gaussian profile fit) to select which line parameters to report. For lines with hyperfine structure we gave preference to the multiple-constrained-Gaussian fit over the single-Gaussian fit, for the other lines, we gave preference to the single-Gaussian fit over the double unconstrained Gaussian fit. We report in the catalog parameters from the 'preferred' fit when its probability was $> 1\%$. If this probability was $< 1\%$, then the 'non-preferred' fitting parameters were reported, but only if they had a fit probability greater than the probability of the preferred fit. If this wasn't the case, then we report the preferred fit, regardless of its fit probability.

Included in the catalog is a detection flag ('D') to indicate the significance of the detection: it is set to 'Y' when the line is well detected ($T_{SNR} > 1$ and $II_{SNR} > 4.0$), 'M' when the detection is marginal ($T_{SNR} > 1$ and $3.0 < II_{SNR} < 4.0$), and 'N' when there is no reliable detection ($T_{SNR} < 1$ or $II_{SNR} < 3.0$). We indicate the number of gaussians in the selected fit via the flag, 'NG'; the values correspond to: 1 for a single Gaussian profile fit, 2 for the two-component unconstrained Gaussian profile fit, 3 for a fit that includes the hyperfine structure, and -1 when no good fit was determined. When the best fit determined was the two-component unconstrained Gaussian profile ('NG'= 2), we report in the catalog values for T_A^*, V_{LSR}, and ΔV (and their uncertainties) derived from a moment (intensity weighted) calculation of the combined line profiles. In many cases, these spectra show clear self-absorption and evidence for outflow/infall motions.

3.4.4 Spectrum residuals

With the best-fit profile selected and subtracted, we then determined the standard deviation in the residuals across both the fit range (R_f) and the complete spectrum (R_s). The former parameter (R_f) reports the ratio in the standard deviation in the residual spectrum in the fit range to that determined from a signal-free portion of the spectrum. Visual inspection of the spectra showed that values for $R_f \gtrsim 1.5$ indicate cases where there is significant emission or absorption remaining in the fit range after the best-fit profile has been removed. As such, we use a value for R_f of $\gtrsim 1.5$ to designate those spectra with 'high residuals'. This parameter helps identify spectra that show non-Gaussian profiles indicative of self-absorption or infall/outflow motions. We indicate cases where $R_f > 1.5$ in the catalog by setting the 'high residuals (HR)' flag to 1.

The second parameter, R_s, reports the number of channels in the residual spectrum that are $> 3\sigma$ after removal of all best-fit profiles. This parameter is useful for identifying spectra that contain other velocity components within the spectrum that were missed by the automated component selection and fitting routine. A high value of R_s indicates either very broad lines or more than two velocity components. High values for this parameter (i.e., > 70) are typically seen toward clumps

in the Galactic Centre where the emission is complex and not well fit by Gaussian profile(s).

3.4.5 Opacities

For all clumps in which the N_2H^+ emission could be fit with a three component Gaussian profile (i.e. in 2256 cases) we have derived an optical depth (τ) of the main hyperfine component ($J'F_1'F' \rightarrow JF_1F = 123 \rightarrow 012$). Assuming LTE, where the excitation temperatures of the three components are the same, we follow the description outlined in Shirley et al. (2005) and calculate the optical depth of the main hyperfine component by taking the ratios of the observed antenna temperatures of the Left and Right components to the Main component. The optical depth was determined numerically by finding the minimum of the function

$$f(\tau) = \left(2 - \left(\frac{T_L(1-e^{-\tau})}{T_M(1-e^{-r_L\tau})}\right)^2 - \left(\frac{T_R(1-e^{-\tau})}{T_M(1-e^{-r_R\tau})}\right)^2\right)^2$$

over the range $-3 < \tau < 6$, where T_L, T_M, and T_R are the fitted T_A^* amplitudes for the Left, Main, and Right components respectively (i.e. the 101-012, 123-012, and 112-012 hyperfine components respectively; these are labeled by their strongest $J'F_1'F' \rightarrow JF_1F$ transitions) and r_L and r_R are the relative intensities calculated based on the each clump's line width (see Shirley et al. 2005 for a details on how these are calculated).

3.5 Synthetic Spectra

To determine the completeness and reliability of the detections reported in the catalog, we generated a series of synthetic spectra which were passed through the same automated line-fitting procedure as described above. For this analysis we assume that there is a single Gaussian component in each spectrum (i.e., that there is one velocity component along the line of sight), that all profiles are Gaussian, and that the simulated emission arises from a molecular transition that shows no hyperfine splitting. All values for, or derived from, the synthetic spectra have the subscript 'syn'.

The synthetic spectra were based on noise spectra drawn randomly from the MALT90 maps for $HC^{13}CCN$, $^{13}C^{34}S$, and H 41α (these maps were selected since the emission from these transitions were rarely detected). A candidate noise spectrum was generated by averaging spectra in a 3×3 pixel box selected randomly according to the distribution of ATLASGAL clump peak positions within the MALT90 maps. The noise spectrum was passed through the baseline subtraction and Gaussian fitting procedure; if a signal was detected with peak amplitude greater than 1.5 times the σ_{noise} of the spectrum then that noise spectrum was rejected. Amplitudes of an accepted candidate noise spectrum were then multiplied by −1.0 to produce a final noise spectrum for use in the analysis. The output of this process was an ensemble of 10,000 noise spectra that statistically sampled the maps with the same weighting in relevant parameters (e.g., observing conditions, galactic longitude, and position within the maps) as the spectra extracted toward each clump.

3.5.1 Completeness

To study the completeness of the reported detections, we superposed Gaussian profiles on the noise spectra and then passed these synthetic spectra through the automated line-fitting procedure. Values for the peak antenna temperature (T_{syn}) were selected uniformly from 0.0 to 1.0 K; values for the line-width (ΔV_{syn}) were selected uniformly from 1.6 to 5 km s^{-1}; and values for the central velocity (V_{syn}) were selected randomly from the range ±150 km s^{-1}. The consensus velocity was set randomly in the range ± 3 km s^{-1} around V_{syn}. These were chosen as they represent the typical values and ranges for these parameters measured within the survey data. We use the same detection criteria for the synthetic spectra as we applied to the real data: a synthetic profile was considered to be 'detected' if the II_{SNR} was > 4, and the T_{SNR} > 1. We impose one additional criteria for the synthetic spectra: that the derived central velocity from the Gaussian profile fit was within ± 1 km s^{-1} of the input V_{syn}.

We used the synthetic spectra to study the fraction of sources detected (completeness) as a function of our detection criteria. The upper panel of Figure 10 shows completeness as a function of $T_{SNR,syn}$ (i.e. T_{syn}/σ_{noise}); the middle panel shows completeness as a function of the ratio of $II_{SNR,syn}$ (i.e. II_{syn}/σ_{noise}). In both panels, the dashed curve corresponds to the expanded scale shown on the right. The dotted vertical lines mark a $T_{SNR,syn}$ of 1 and an $II_{SNR,syn}$ of 3 and 4, which correspond to the criteria imposed for detections to be included within the catalog.

We find that the completeness versus $T_{SNR,syn}$ rises rapidly, a consequence of the peak-fitting algorithm starting from the highest amplitude channel in the search region. Completeness versus $II_{SNR,syn}$ rises somewhat more slowly, reaching 80% by $II_{SNR,syn}$=4 and 99% by $II_{SNR,syn}$=8. The lower panel of Figure 10 shows the completeness as a function of T_{syn}. Since T_{syn} in these spectra represents the measured T_A^* from our data, these results indicate that we achieve a completeness of >95% for detections with a measured T_A^* > 0.4 K and > 99% for detections with a T_A^* > 0.6 K.

3.5.2 Reliability

Passing the noise spectra through our standard analysis procedure provided a measure of the reliability of detections, i.e., the probability of an accidental (false-positive) detection, as a function of detection criteria.

Figure 11 shows the normalized cumulative distribution in II_{SNR} determined from the noise spectra (note, this will characterize accidental detections due to noise and baseline fluctuations). The probability of a false-positive detection is $< 0.3\%$ for an $II_{SNR} > 3$.

By comparing the fitting results with the known characteristics used to generate the synthetic profiles we have also determined the reliability with which the fitting procedure recovers the Gaussian parameters: amplitude, velocity, line-width, and integrated intensity, and the accuracy with which it estimates their uncertainties. Figure 12 compares the derived parameters to the input values (panels are amplitude, line-width, velocity, and integrated intensity, respectively, from upper to lower). For the amplitude, line-width, and integrated intensity we calculate the ratio of derived values to input values; for the velocity, we calculate the difference. For input $T_{syn} > 0.24$ K, the distributions are close to unity, which indicates that the fitting procedure accurately determines all three Gaussian parameters (amplitude, line width, and integrated intensity) and introduces no significant bias in its estimations. Indeed, the relative uncertainty in these quantities, as estimated by the standard deviations of the ratios from unity (shown as the error bars), was $\sim$20% for $T_{syn} \sim 0.24$ K and improved to $< 5\%$ for $T_{syn} > 1$ K.

4 DESCRIPTION OF THE CATALOG

The catalog contains an entry for each of the clumps covered by the MALT90 survey. While the total number of spectra extracted toward the clumps is 3246, in 311 cases there were two distinct velocity components detected along the line of sight. In these cases we report separate entries ('A' and 'B' components) which leads to a total of 3557 entries in the catalog.

Table 2 gives a sample of a subset of the catalog entries. For brevity, we include here, as an example, a description of the derived properties for HCO^+ (1–0). The full catalog contains the same entries (i.e., columns 10–25) repeated for each of the 16 transitions covered by the survey. The complete catalog is available at www.malt90.catalog.location.

The columns of Table 2 are as follows:

(1) the clump name (from the ATLASGAL catalogs Contreras et al. 2013 and Urquhart et al. 2014), appended with an 'S', 'A', or 'B'; (2) and (3) the Galactic coordinates of the clumps' ATLASGAL 870 μm emission peak (ℓ, b, in degrees); (4) the ATLASGAL 870 μm peak flux (in Jy); (5) the IR-based category assigned to the clump (S), 'Q' for quiescent, 'A' for protostellar, 'C' for compact H II regions, 'H' for extended H II regions, 'P' for photo-dissociation regions, or 'U' for uncertain; (6) the consensus velocity (V_C in km s^{-1}) determined as the intensity weighted velocity derived from reliable fits to HCO^+, HCN, and N_2H^+; (7) the total number of lines detected toward this clump with $II_{SNR} > 3.0$ (NL); (8) and (9) the measured opacity (τ) and its uncertainty; (10) the flag indicating whether emission was detected (D), 'Y' when the line is well detected ($II_{SNR} > 4.0$), 'M' when the detection is marginal ($3.0 < II_{SNR} < 4.0$), and 'N' when there is no reliable detection; (11) the flag indicating the number of Gaussian profiles that were fit (NG), 1 for a single Gaussian profile fit, 2 for the two-component unconstrained Gaussian profile fit, 3 for a fit that includes the hyperfine structure, and -1 when no good fit was determined; (12) and (13) the derived antenna temperature and its uncertainty from the Gaussian fitting (T_A^*, in K); (14) and (15) the derived velocity and its uncertainty from the Gaussian fitting (V_{LSR}, in km s^{-1}); (16) and (17) the derived velocity FWHM and its uncertainty from the Gaussian fitting (ΔV, in km s^{-1}) ; (18) and (19) the integrated intensity (II, in K km s^{-1}) and its uncertainty; (20) the 1 σ rms noise of the spectrum (σ_{noise} in km s^{-1}); (21) the fit probability; (22) the integrated intensity signal-to-noise ratio (II_{SNR}); (23) the ratio in the standard deviation in the residual spectrum in the fit range to that determined from a signal-free portion of the spectrum (R_f); (24) the flag indicating if the profile has a high residual in the fit range, $R_f > 1.5$ (HR); (25) the total number of channels in the residual spectrum that are $> 3\,\sigma$ after removal of all best-fit profiles (R_s).

5 EXAMPLES: IMAGES AND SPECTRA

Figures 1–8 provide an overview of the ATLASGAL/*Spitzer* images and MALT90 spectra toward a selection of clumps that are contained within the catalog. We show here clumps that are representative of those in each of the IR-based categories: Figure 1 shows a quiescent clump, Figure 2 a protostellar clump, Figures 3 and 5 H II regions, and Figure 5 a PDR. Moreover, in Figures 6 and 7 we also show an example of when 2 separate components were detected along the line of sight toward an ATLASGAL clump ('A' and 'B' components), and in Figure 8 we shown an example of a clump that is located in the Galaxy's Central Molecular Zone.

In all cases these figures show an ATLASGAL 870 μm dust continuum image, two *Spitzer* three colour images (combining the 3–8 μm and 3–24 μm data), and panels showing the MALT90 spectra, fits, and residuals for each emission line. If emission was detected, the derived parameters from the best-fit Gaussian profile are labelled, the red line shows this best-fit profile. The consensus velocity is marked as the solid vertical line.

Quiescent clumps (e.g., Fig. 1) are categorised as bright in the 870 μm dust continuum emission (top left image) and dark at 3–24 μm (top middle and right images), indicating that the dust is very cold and dense. As expected, these clumps typically have detections only from the four dense gas tracers of HCO^+ HNC, N_2H^+,

and HCN (this example also shows a marginal detection of $H^{13}CO^+$) and no detections from the high excitation lines. In this example, both the N_2H^+, and HCN hyperfine components were reliably fit with a three-component Gaussian profile. For all spectra toward this clump the fit residuals are low ($R_f < 1.5$) and the measured V_{LSR} are consistent with the derived consensus velocity. Moreover, consistent with its lack of star-formation, the line emission from this clump has relatively narrow line-widths ($\sim 2.1\,\mathrm{km\ s^{-1}}$).

In contrast, toward typical protostellar clumps (e.g., Fig. 2) which show obvious IR signatures of active star-formation such as extended $4.5\,\mu$m emission tracing shocked gas (colour-coded as green in the top middle image) and bright $24\,\mu$m emission tracing an embedded protostar (colour-coded as red in the top right image), the suite of 90GHz transitions are well detected, and in many cases the emission is bright, with complex line profiles. In this example, N_2H^+ hyperfine components are resolved, so this emission is well-fit by a three-component Gaussian profile. For HCO^+, HNC, and HCN, however, the profiles are clearly non-Gaussian, so while a single component was found to be the 'best-fit' to these profiles, there are clearly significant residuals remaining in the spectrum: in these cases the reported R_f values are 3.8–6.0. A comparison between the profiles of the optically thick and thin transitions (i.e., HCO^+ and $H^{13}CO^+$ or HNC and $HN^{13}C$) indicate that the optically thick transitions show self-absorption and, thus, may be tracing infall/outflows motions within the gas. Moreover, the detection of the high excitation lines toward this clump (i.e., HNCO, CH_3CN, and HC_3N) suggests that the gas is heated from a newly formed protostar and confirms active star-formation within this clump. Moreover, the detection of broad SiO emission independently confirms widespread shocks within it.

Toward typical H II regions (e.g., Fig. 3) which have bright 3–$24\,\mu$m emission, indicative of embedded, active star formation, the suite of 90GHz transitions are also well detected. The line emission toward H II regions tends to be bright, with complex line profiles, similar to protostellar clumps. Differences can be seen, however, in the relative intensities of several of the lines for these two categories (e.g., compare the line strengths of the isotopologues, higher excitation lines, and the SiO emission in Figs. 2 and 3). The differences in the relative intensities of these lines highlight differences in the chemistry and the physical conditions within these two types of clumps.

While not widespread within the survey, H 41α emission was detected toward 22 clumps (0.6% of the full sample). Since H 41α traces ionized gas, presumably from an embedded high-mass star that is emitting UV radiation, its detection pinpoints a later phase in the evolution for these clumps. Figure 4 shows an example of a clump, and its associated IR emission, that has bright, reliable detection of H 41α ($\mathrm{II_{SNR}} = 25$).

Clumps that appear to be associated with a PDR (e.g., Fig. 5) were separated into their own IR-based category, since they are likely associated with very different conditions within the gas compared to the other quiescent clumps, protostellar clumps, and H II regions. Because PDRs are regions illuminated along the edge of a molecular cloud by nearby UV radiation from a high-mass star, clumps located within them are likely to be externally heated and potentially dominated by shock and PDR chemistry. Indeed, in the example shown in Figure 5, we find that although there appears to be no IR emission directly associated with the bright dust emission, we see line emission from many of the higher excitation transitions and SiO which indicates that the gas is heated and shocked. While these clumps are valuable to study in detail to learn about star-formation that is potentially triggered on the edge of a molecular cloud, we exclude these clumps from the analysis and discussion around evolution, since it is unclear if they can be used to describe a single phase in the evolutionary sequence for these clumps.

Figures 6 and 7 show an example of a clump (in this case a protostellar clump) that has two distinct velocity components detected toward it. Component A, shown in Figure 6, is well detected in the lines of HCO^+, HNC, N_2H^+, and HCN (and C_2H), while component B, shown in Figures 7, is well detected in the first three of these lines. In all cases the profiles are well-fit and the two components well-separated in velocity.

The final example, in Figure 8, shows the line emission toward a clump located in the Galaxy's Central Molecular Zone (CMZ). Note the very broad line profiles, $\Delta V \sim 17$–$27\,\mathrm{km\ s^{-1}}$, which are due to the high levels of turbulence that characterise clumps located in the CMZ. While this clump appears to be IR-dark and, as such, is classified as 'quiescent', many of the higher excitation lines, including SiO, are also detected toward it. Since the bulk of the gas in the CMZ has temperatures of $\sim$ 80K and densities $> 10^4\,\mathrm{cm^{-3}}$ (Walmsley et al. 1986; Ao et al. 2013), many of the higher excitation lines (like those covered by MALT90) show bright, widespread emission across the region. This has lead to the speculation that perhaps shock chemistry dominates in the CMZ (Wilson et al. 1982; Martín-Pintado et al. 2001). As such, we also exclude clumps located in the CMZ from the analysis and discussion of evolution, since their chemistry is likely very different from the rest of the MALT90 clumps that are located throughout the Galactic disk.

6 ENSEMBLE PROPERTIES

6.1 The MALT90 sample: representative of typical cluster-forming clumps

ATLASGAL was a systematic, un-biased survey of dust continuum emission with the goal of identifying and characterising high-mass clumps within the Galaxy (Schuller et al. 2009). As such, the catalogues derived from this survey represent an excellent database for detailed studies of these clumps.

The MALT90 survey targeted 3246 clumps that were identified within ATLASGAL. To demonstrate that the MALT90-selected clumps are representative of the larger ATLASGAL sample, Figure 13 shows histograms of the 870 μm peak flux from ATLASGAL for the clumps included within MALT90 (thin histogram), along with the ATLASGAL sample for comparison (thick histogram). MALT90 observed almost all ($\sim$ 90%) of the ATLASGAL clumps with fluxes $>$ 1 Jy, and $\sim$ 60% of the ATLASGAL clumps with fluxes between 0.25 and 1 Jy. Those ATLASGAL clumps that were not included within MALT90 are typically located within the Galaxy's CMZ or in the 1st Galactic quadrant: MALT90's primary goal was to cover all clumps within the 4th Galactic quadrant.

The panels of Figure 13 also shows the 870 μm flux distribution for the MALT90 clumps separated by the number of lines detected toward them (i.e., NL $\geq$ 1, 4, 6, and 8, from upper to lower panels, respectively; dotted histograms). We find that the clumps with no detected lines (160 in total) are the fainter 870μm clumps (see the upper panel of Fig. 13), while those with multiple lines detected toward them are amongst the brightest 870 μm clumps (see the lower panels in Fig. 13).

The trend of brighter 870μm clumps having a higher number of lines detected toward them is also seen when the MALT90 sample is separated into the IR-based categories (see Fig. 14). Regardless of the category, the brightest 870 μm clumps within each group have a higher fraction of lines detected toward them. Moreover, those that have no detected emission tend to be at the fainter end of the ATLASGAL flux distribution.

6.2 Detection statistics

In addition to listing information about the emission lines observed as part of the MALT90 survey, Table 1 also summarises the detection rates for each line[2]. We find that the detection rates are highest for the four (1–0) molecular transitions of HCO^+, HNC, N_2H^+, and HCN ($\sim$72–88%). A small number of clumps are detected in the lines of $^{13}C^{34}S$, $HC^{13}CCN$, and H 41α (9, 10 and 22 respectively); the number of clumps detected in each line is listed in Table 1.

Figure 15 shows that most clumps ($\sim$ 95%) are detected in at least one line. Just under half of the clumps ($\sim$ 48%) are detected in 4 or more lines, while only 2 clumps are detected in 13 or more lines (clumps AGAL351.444+00.659_S and AGAL000.666-00.034_B have 13 and 14 detections, respectively).

Figure 16 show the normalised cumulative distribution of the T_{SNR} and II_{SNR} for each of the emission lines. The vertical dotted lines in all panels mark the cuts used to define detections for inclusion in the catalog (i.e., $T_{SNR} > 1$ and $II_{SNR} > 3$, in the case of marginal detections, or $T_{SNR} > 1$ and $II_{SNR} > 4$ in the case of reliable detections). Flat curves in these plots (e.g., the II_{SNR} curves for HCO^+, HNC, N_2H^+, HCN, SiO, HNCO, CH_3CN, and H 41α) imply that the inclusion or exclusion of detections is insensitive to the exact choice of the selection criteria. In contrast, for curves that rise steeply (e.g., the II_{SNR} curves for C_2H, $H^{13}CO^+$, HC_3N, $HN^{13}C$, and ^{13}CS), the exact choice of the selection criteria does significantly affect the number of detections that are included in the catalog. To avoid unnecessary exclusion of possible detections, we mark in the catalog all detections with a derived $3 < II_{SNR} < 4$ as 'marginal'. Note that the selection criteria of $T_{SNR} > 1$ has little effect, since almost all lines have values greater than this. However, this cut was imposed as part of the selection of reliable detections to avoid the inclusion of very broad lines that have a high integrated intensity, but are not discernible above the noise in T_A^* (i.e, any remaining slowly varying baselines).

The upper panel of Figure 17 shows the percentage of clumps that were detected in each of the emission lines. As expected, the highest detection rates of the lines covered by MALT90 arise from the (1–0) transitions of HCO^+, HNC, N_2H^+, and HCN. Of the istopologues, $H^{13}CO^+$ has the highest detection rate, followed by $HN^{13}C$. The molecular transition, C_2H, is also well detected toward the clumps ($\sim$ 47%).

The middle panel of Figure 17 shows the percentage of clumps with detections for each emission line, separated out by the number of Gaussian profiles that were fit to the spectrum (i.e., 1, 2, or 3; dark grey, grey, and light grey bars respectively). In the majority of cases for transitions without hyperfine splitting, the best-fit was found when fitting a single Gaussian profile to the emission (dark grey bars). For transitions with hyperfine splitting (N_2H^+, HCN, and C_2H), the best-fit was most often found when it included the known hyperfine structure (light grey bars). However, in a small number of cases a single Gaussian profile was found to produce the best-fit; this occurred when the line widths were large and the individual hyperfine components could

[2]these percentages are calculated with respect to the 3557 entries within the catalog

not be easily separated ($\sim$ 7%, $\sim$ 17% and $\sim$ 0.1% for N_2H^+, HCN, and C_2H respectively).

The lower panel of Figure 17 shows the percentage of clumps with detections for each molecular transition, separated out by the significance of the residual that remains after the best-fit profile(s) are removed. Dark grey bars show the percentage of clumps for which the residuals are low (i.e., HR=0); light grey bars indicate the percentage where the residuals are high (HR=1). The spectra from HCO^+ show the highest percentage of those with high residuals, which is expected since this molecular transition typically has the highest optical depth of those included in the survey (e.g., Sanhueza et al. 2012; Hoq et al. 2013). As such, HCO^+ is therefore an excellent tracer of outflow and infall motions that give rise to non-Gaussian line profiles.

6.3 Distributions of the derived parameters

To determine whether the various molecular transitions are tracing similar or distinct physical regions, we have plotted in Figure 18 the distribution functions of the ratio of integrated intensity (II) to the mean Integrated Intensity (II/mean(II); left), line-width (ΔV; middle), and the difference between the derived velocity and the consensus velocity (V–V_C; right), for a subset of the detected molecular transitions.

As might be expected for optically thicker molecular transitions (e.g., HCO^+, HNC, N_2H^+, and HCN) show a relatively broader integrated intensity distribution compared to the optically thinner molecular transitions (e.g., $H^{13}CO^+$, $HN^{13}C$, and ^{13}CS). Since an optically thick transition will be sensitive to a range of column densities, a broad distribution in their integrated intensities would be expected. Moreover, since the rarer isotopologues will trace material in the inner, dense regions of the clumps, we would expect a narrower range in the distribution in their integrated intensities. The higher excitation lines (i.e., HNCO, CH_3CN, HC_3N, C_2H, and SiO) all show a very broad distribution in their integrated intensities. This likely reflects the very different conditions (e.g., shocks, high excitation temperatures) of the gas within which these molecular lines are excited.

The line widths are in general narrowest for the isotopologues (e.g., $H^{13}CO^+$, $HN^{13}C$, ^{13}CS), compared to the optically thicker transitions (e.g., HCO^+, HNC, and HCN). The largest linewidths are found for the highest excitation energy transitions, which tend to be excited in regions of active star formation (e.g., CH_3CN, HNCO, and SiO). For SiO it is clear that these broad line-widths are due to the formation of SiO in shocks. The broad line widths of HNCO and CH_3CN confirms that these molecular transitions are also shock-tracers. Note, that the very broad line-widths, i.e. $> 10\,\mathrm{km\ s^{-1}}$, arise from the sub-set of clumps located within the Galaxy's Central Molecular Zone (CMZ) where high levels of turbulence and shocks dominate.

Finally, the small difference between the derived velocity and the consensus velocity within individual clumps reveals that the molecular emission is generally well centred at the consensus velocity. This implies that the emission from the various molecules arise from within the same physical regions. The one exception is CH_3CN, for which the distribution is centred at a velocity about $-4\,\mathrm{km\ s^{-1}}$ from the derived consensus velocity. This may indicate an error in our assumed rest frequency of CH_3CN or that the Gaussian profile was fit to a blend of the CH_3CN K=0 and K=1 hyperfine components. The broadest distribution in the derived velocities relative to the consensus velocities also occurs for the transitions with the highest line-widths: CH_3CN, HNCO, and SiO. This may indicate distinctly different velocities of the shocked gas, and/or the difficulty in establishing an accurate central velocity in the presence of large line-widths.

6.4 Trends as a function of evolution

We use the IR-based categories to broadly represent three stages in the evolution of a clump with increasing levels of star-formation; quiescent clumps represent an early phase before star-formation has begun, protostellar clumps show the initial signatures of active star formation, while H II regions represent a later stage when young, high-mass stars have already formed. Given the harsh environment and complexity of the chemistry within the Galaxy's CMZ compared to the Galactic disk, we exclude from the plots and analysis in this section all clumps that fall within $\pm$ 10 degrees in Galactic Longitude of the Galactic Centre.

Also overlaid on Figure 15 are the percentages of quiescent and protostellar clumps with $>$ n detections (right axis; dashed and dot-dashed lines, respectively). For simplicity we include on this plot the curves for the quiescent and protostellar clumps: the sample of H II regions show a similar curve to the protostellar clumps. We find that clumps with active star formation, have a higher percentage of detections compared to the full survey and those clumps that are more quiescent. Moreover, the protostellar clumps and H II regions are detected in 4 or more lines more frequently ($\sim$60% and $\sim$53%, respectively) compared to the full survey ($\sim$ 48%) and the quiescent clumps ($\sim$ 35%). This trend with evolution is expected since the gas is likely hotter and denser in the more evolved star-forming clumps and, thus, more readily detected in the 90 GHz lines.

Figure 19 shows the detection rates for most emission lines as a function of the IR-based category for each clump. The categories are shown on the x-axis increasing in evolutionary sequence from left to right: quiescent clumps, protostellar clumps, and H II regions. Shown

as the dotted line in each panel is the percentage of clumps detected within the survey for each of the classifications (19%, 22%, and 21%, respectively). We find that the detection rates within each category for the four molecular transitions of HCO^+, HNC, N_2H^+, and HCN follows well the overall detection rates for the full survey (see the top four panels in Fig. 19). In contrast, the isotopologues and the higher excitation lines (e.g. $H^{13}CO^+$, $HN^{13}C$, HNCO, CH_3CN, HC_3N, and SiO) are typically detected less frequently toward 'quiescent' clumps and more frequently toward those that are actively star-forming (i.e. the 'protostellar' clumps and H II regions) compared to the overall survey.

These trends are exactly what is expected if these categories reflect the evolution of the clumps: as the level of star-formation activity increases, the gas will become hotter and denser and, thus, the tracers of these conditions will be more readily detected. Indeed, this evolutionary sequence is reinforced by the clear trend in the detection rates for H 41α emission (see the lower panel of Fig. 19). Since this emission traces ionized gas, presumably from an embedded high-mass star, it should only be observed when the central high-mass star has turned on, in the later H II region phase.

To assess whether the ensemble of properties for the different molecular transitions varies with evolutionary stage, Figure 20 compares ratios of integrated intensity (left column), ratios of line-widths (middle column), and the differences of the central velocity (right column) for various pairs of transitions as a function of the IR-derived categories for the clump. These plots reveal several interesting trends. Firstly, the integrated intensity ratios of HCO^+/HNC and HCN/HNC increase with evolutionary stage (left column). These trends probably indicate the fact that HNC is relatively more abundant in colder, less evolved clumps than those that show active star-formation (e.g. see Hoq et al. 2013). Secondly, the integrated intensity ratios of HCO^+/N_2H^+, HNC/N_2H^+, and C_2H/N_2H^+ are typically higher in the H II region phase, indicating that N_2H^+ is relatively brighter in the colder earlier stages, and is consistent with the notion that N_2H^+ resists freezing onto dust grains more effectively than other molecules (Stephens et al. 2015; Sanhueza et al. 2012).

The $HCO^+/H^{13}CO^+$ and $HNC/HN^{13}C$ integrated intensity ratios also tend to increase with increasing evolutionary stage. We surmise that this trend indicates a decreasing optical depth as the clumps evolve, which is consistent with both our measurements of τ (see Fig. 21) and the results of Guzmán et al. (2015) which show a trend of lower clump column densities in the more evolved stages.

The ratios of line-widths show no obvious trends with evolution (middle column). However, differences in the derived velocities (right column) clearly show that the HCO^+ emission is blue-shifted with respect to the emission from the other molecular transitions (e.g., HNC, N_2H^+, and SiO): the difference is largest at the earliest quiescent stage and monotonically decreases as the clumps evolve. Especially striking is the trend in the $HCO^+ - H^{13}CO^+$ velocities. This result suggests that the optically thickest HCO^+ emission shows a 'blue-red asymmetry' that indicates overall collapse. This trend was noted from a sub-set of the MALT90 survey data in (He et al. 2015). The blue-red asymmetry of the HCO^+ emission detected from the full survey will be discussed in a future paper (Jackson et al., in prep.).

7 SUMMARY

Targeting 3246 high-mass clumps identified in the ATLASGAL 870 μm Galactic Plane Survey that span a range in star-formation activity, the MALT90 survey aims to characterise the physical and chemical evolution of dense, high-mass clumps. By simultaneously mapping emission from 16 different species that trace specific physical and chemical conditions, the MALT90 survey provides a wealth of information about the global characteristics of the gas within these clumps. This paper describes the first catalog from MALT90 generated to summarise the properties of the emission detected toward each of the clumps.

In order to characterise the detected emission toward each clump, we have first extracted a single spectrum toward each ATLASGAL peak for each of the emission lines, then have fit each of these spectra with either a single or multiple Gaussian profile(s). Having determined the best-fit profile, we report in the catalog 16 derived values and flags for each of the 16 emission lines. We describe the catalog entries and include a sub-set of its content here, the full catalog contains 263 columns for each of the 3557 entries and is available online at www.malt90.catalog.location.

Using synthetic spectra we estimate that the catalog has: a completeness of >95% for detections with a measured $T_A^* > 0.4$ K and > 99% for detections with a $T_A^* > 0.6$ K, a probability of a false-positive detection of < 0.3% for an $II_{SNR} > 3$, and a relative uncertainty of the measured quantities of < 20% over the range of detection criteria.

We find that the detection rates are highest for the (1–0) molecular transitions of HCO^+, HNC, N_2H^+, and HCN (∼72–88%). The majority of clumps (∼ 96%) are detected in at least one of the lines, just under half of the clumps (∼ 48%) are detected in 4 or more lines, while only 2 clumps are detected in 13 or more lines. We find that HCO^+ spectra typically show non-Gaussian profiles (indicated by a high residual in the spectrum after the best-fit Gaussian is subtracted), which is expected since this molecular transition typically has the highest optical depth, and is therefore an excellent tracer of out-

flow and infall motions that give rise to non-Gaussian profiles.

For each clump, we determine a single 'consensus' velocity (V_C) to describe its associated line emission. Deriving a consensus velocity is important since it will be used to determine kinematic distances to each clump (Whitaker et al. in prep.) and, hence, their masses and luminosities (Contreras et al. in prep.). The difference between individually-derived velocities and the consensus velocity within individual clumps reveals that despite the exact excitation conditions, most of the line emission is generally well centred around the consensus velocity. This implies that the emission from the various species arise from within the same physical regions.

We broadly classify the clumps into groups based on their IR signatures. We find that clumps with active star formation (i.e., those classified as either protostellar or H II regions), have a higher percentage of detections for most emission lines compared to the full survey and those clumps that appear to be more quiescent. Moreover, the protostellar clumps and H II regions are detected in 4 or more lines more frequently (∼60% and ∼53%, respectively) compared to the full survey (∼48%) and the quiescent clumps (∼35%).

We find several interesting trends in the ensemble of properties for the different molecular transitions when plotted as a function of the clumps' evolutionary state. From trends in the integrated intensity ratios, we find that (1) HNC is relatively brighter in colder, less evolved clumps than those that show active star-formation, (2) N_2H^+ is relatively brighter in the earlier stages, and (3) that the observed optical depth decreases as the clumps evolve. Trends in the velocity differences show a particularly striking result: the optically thickest HCO^+ emission shows a 'blue-red asymmetry' that indicates overall collapse that monotonically decreases as the clumps evolve.

This catalog represents the largest compiled database of line emission toward high-mass clumps. As such, it is a valuable data set for studies of these clumps and provides a definitive source list for ALMA observations of the small-scale structure within high-mass clumps.

8 ACKNOWLEDGEMENTS

The MALT90 project team gratefully acknowledges the use of dense clump positions supplied by ATLASGAL. ATLASGAL is a collaboration between the Max Planck Gesellschaft (MPG: Max Planck Institute for Radioastronomy, Bonn and the Max Planck Institute for Astronomy, Heidelberg), the European Southern Observatory (ESO) and the University of Chile. This work was supported by NSF grant AST-1211844. A.E.G. acknowledges support of CONICYT through FONDECYT 3150570.

Facilities: Mopra.

REFERENCES

Aguirre, J. E., Ginsburg, A. G., Dunham, M. K., Drosback, M. M., Bally, J., Battersby, C., Bradley, E. T., Cyganowski, C., Dowell, D., Evans, II, N. J., Glenn, J., Harvey, P., Rosolowsky, E., Stringfellow, G. S., Walawender, J., & Williams, J. P. 2011, ApJS, 192, 4

Ao, Y., Henkel, C., Menten, K. M., Requena-Torres, M. A., Stanke, T., Mauersberger, R., Aalto, S., Mühle, S., & Mangum, J. 2013, A&A, 550, A135

Benjamin, R. A., Churchwell, E., Babler, B. L., Bania, T. M., Clemens, D. P., Cohen, M., Dickey, J. M., Indebetouw, R., Jackson, J. M., Kobulnicky, H. A., Lazarian, A., Marston, A. P., Mathis, J. S., Meade, M. R., Seager, S., Stolovy, S. R., Watson, C., Whitney, B. A., Wolff, M. J., & Wolfire, M. G. 2003, PASP, 115, 953

Carey, S. J., Noriega-Crespo, A., Mizuno, D. R., Shenoy, S., Paladini, R., Kraemer, K. E., Price, S. D., Flagey, N., Ryan, E., Ingalls, J. G., Kuchar, T. A., Pinheiro Gonçalves, D., Indebetouw, R., Billot, N., Marleau, F. R., Padgett, D. L., Rebull, L. M., Bressert, E., Ali, B., Molinari, S., Martin, P. G., Berriman, G. B., Boulanger, F., Latter, W. B., Miville-Deschenes, M. A., Shipman, R., & Testi, L. 2009, PASP, 121, 76

Churchwell, E., Babler, B. L., Meade, M. R., Whitney, B. A., Benjamin, R., Indebetouw, R., Cyganowski, C., Robitaille, T. P., Povich, M., Watson, C., & Bracker, S. 2009, PASP, 121, 213

Contreras, Y., Schuller, F., Urquhart, J. S., Csengeri, T., Wyrowski, F., Beuther, H., Bontemps, S., Bronfman, L., Henning, T., Menten, K. M., Schilke, P., Walmsley, C. M., Wienen, M., Tackenberg, J., & Linz, H. 2013, A&A, 549, A45

Foster, J. B., Jackson, J. M., Barnes, P. J., Barris, E., Brooks, K., Cunningham, M., Finn, S. C., Fuller, G. A., Longmore, S. N., Mascoop, J. L., Peretto, N., Rathborne, J., Sanhueza, P., Schuller, F., & Wyrowski, F. 2011, ApJS, 197, 25

Foster, J. B., Rathborne, J. M., Sanhueza, P., Claysmith, C., Whitaker, J. S., Jackson, J. M., Mascoop, J. L., Wienen, M., Breen, S. L., Herpin, F., Duarte-Cabral, A., Csengeri, T., Contreras, Y., Indermuehle, B., Barnes, P. J., Walsh, A. J., Cunningham, M. R., Britton, T. R., Voronkov, M. A., Urquhart, J. S., Alves, J., Jordan, C. H., Hill, T., Hoq, S., Brooks, K. J., & Longmore, S. N. 2013, PASA, 30, 38

Guzmán, A. E., Sanhueza, P., Contreras, Y., Smith, H. A., Jackson, J. M., Hoq, S., & Rathborne, J. M. 2015, ApJ, 815, 130

He, Y.-X., Zhou, J.-J., Esimbek, J., Ji, W.-G., Wu, G., Tang, X.-D., Yuan, Y., Li, D.-L., & Baan, W. A. 2015, MNRAS, 450, 1926

Hoq, S., Jackson, J. M., Foster, J. B., Sanhueza, P., Guzmán, A., Whitaker, J. S., Claysmith, C., Rathborne, J. M., Vasyunina, T., & Vasyunin, A. 2013, ApJ, 777, 157

Jackson, J. M., Rathborne, J. M., Foster, J. B., Whitaker, J. S., Sanhueza, P., Claysmith, C., Mascoop, J. L., Wienen, M., Breen, S. L., Herpin, F., Duarte-Cabral, A., Csengeri, T., Longmore, S. N., Contreras, Y., Indermuehle, B., Barnes, P. J., Walsh, A. J., Cunningham, M. R., Brooks, K. J., Britton, T. R., Voronkov, M. A., Urquhart, J. S., Alves, J., Jordan, C. H., Hill, T., Hoq, S., Finn, S. C., Bains, I., Bontemps, S., Bronfman, L., Caswell, J. L., Deharveng, L., Ellingsen, S. P., Fuller, G. A., Garay, G., Green, J. A., Hindson, L., Jones, P. A., Lenfestey, C., Lo, N., Lowe, V., Mardones, D., Menten, K. M., Minier, V., Morgan, L. K., Motte, F., Muller, E., Peretto, N., Purcell, C. R., Schilke, P., Bontemps, S.-N., Schuller, F., Titmarsh, A., Wyrowski, F., & Zavagno, A. 2013, PASA, 30, 57

Ladd, N., Purcell, C., Wong, T., & Robertson, S. 2005, PASA, 22, 62

Liu, X.-L., Wang, J.-J., & Xu, J.-L. 2013, MNRAS, 431, 27

Martín-Pintado, J., Rizzo, J. R., de Vicente, P., Rodríguez-Fernández, N. J., & Fuente, A. 2001, ApJ, 548, L65

Miettinen, O. 2014, A&A, 562, A3

Molinari, S., Swinyard, B., Bally, J., Barlow, M., Bernard, J.-P., Martin, P., Moore, T., Noriega-Crespo, A., Plume, R., Testi, L., Zavagno, A., Abergel, A., Ali, B., André, P., Baluteau, J.-P., Benedettini, M., Berné, O., Billot, N. P., Blommaert, J., Bontemps, S., Boulanger, F., Brand, J., Brunt, C., Burton, M., Campeggio, L., Carey, S., Caselli, P., Cesaroni, R., Cernicharo, J., Chakrabarti, S., Chrysostomou, A., Codella, C., Cohen, M., Compiegne, M., Davis, C. J., de Bernardis, P., de Gasperis, G., Di Francesco, J., di Giorgio, A. M., Elia, D., Faustini, F., Fischera, J. F., Fukui, Y., Fuller, G. A., Ganga, K., Garcia-Lario, P., Giard, M., Giardino, G., Glenn, J. ., Goldsmith, P., Griffin, M., Hoare, M., Huang, M., Jiang, B., Joblin, C., Joncas, G., Juvela, M., Kirk, J., Lagache, G., Li, J. Z., Lim, T. L., Lord, S. D., Lucas, P. W., Maiolo, B., Marengo, M., Marshall, D., Masi, S., Massi, F., Matsuura, M., Meny, C., Minier, V., Miville-Deschênes, M.-A., Montier, L., Motte, F., Müller, T. G., Natoli, P., Neves, J., Olmi, L., Paladini, R., Paradis, D., Pestalozzi, M., Pezzuto, S., Piacentini, F., Pomarès, M., Popescu, C. C., Reach, W. T., Richer, J., Ristorcelli, I., Roy, A., Royer, P., Russeil, D., Saraceno, P., Sauvage, M., Schilke, P., Schneider-Bontemps, N., Schuller, F., Schultz, B., Shepherd, D. S., Sibthorpe, B., Smith, H. A., Smith, M. D., Spinoglio, L., Stamatellos, D., Strafella, F., Stringfellow, G., Sturm, E., Taylor, R., Thompson, M. A., Tuffs, R. J., Umana, G., Valenziano, L., Vavrek, R., Viti, S., Waelkens, C., Ward-Thompson, D., White, G., Wyrowski, F., Yorke, H. W., & Zhang, Q. 2010, PASP, 122, 314

Müller, H. S. P., Schlöder, F., Stutzki, J., & Winnewisser, G. 2005, Journal of Molecular Structure, 742, 215

Müller, H. S. P., Thorwirth, S., Roth, D. A., & Winnewisser, G. 2001, A&A, 370, L49

Rathborne, J. M., Longmore, S. N., Jackson, J. M., Alves, J. F., Bally, J., Bastian, N., Contreras, Y., Foster, J. B., Garay, G., Kruijssen, J. M. D., Testi, L., & Walsh, A. J. 2015, ApJ, 802, 125

Rathborne, J. M., Longmore, S. N., Jackson, J. M., Foster, J. B., Contreras, Y., Garay, G., Testi, L., Alves, J. F., Bally, J., Bastian, N., Kruijssen, J. M. D., & Bressert, E. 2014a, ApJ, 786, 140

Rathborne, J. M., Longmore, S. N., Jackson, J. M., Kruijssen, J. M. D., Alves, J. F., Bally, J., Bastian, N., Contreras, Y., Foster, J. B., Garay, G., Testi, L., & Walsh, A. J. 2014b, ApJ, 795, L25

Sanhueza, P., Jackson, J. M., Foster, J. B., Garay, G., Silva, A., & Finn, S. C. 2012, ApJ, 756, 60

Schöier, F. L., van der Tak, F. F. S., van Dishoeck, E. F., & Black, J. H. 2005, A&A, 432, 369

Schuller, F., Menten, K. M., Contreras, Y., Wyrowski, F., Schilke, P., Bronfman, L., Henning, T., Walmsley, C. M., Beuther, H., Bontemps, S., Cesaroni, R., Deharveng, L., Garay, G., Herpin, F., Lefloch, B., Linz, H., Mardones, D., Minier, V., Molinari, S., Motte, F., Nyman, L., Reveret, V., Risacher, C., Russeil, D., Schneider, N., Testi, L., Troost, T., Vasyunina, T., Wienen, M., Zavagno, A., Kovacs, A., Kreysa, E., Siringo, G., & Weiß, A. 2009, A&A, 504, 415

Shirley, Y. L., Nordhaus, M. K., Grcevich, J. M., Evans, II, N. J., Rawlings, J. M. C., & Tatematsu, K. 2005, ApJ, 632, 982

Simpson, G. & Mayer-Hasselwander, H. 1986, A&A, 162, 340

Stephens, I. W., Jackson, J. M., Sanhueza, P., Whitaker, J. S., Hoq, S., Rathborne, J. M., & Foster, J. B. 2015, ApJ, 802, 6

Urquhart, J. S., Csengeri, T., Wyrowski, F., Schuller, F., Bontemps, S., Bronfman, L., Menten, K. M., Walmsley, C. M., Contreras, Y., Beuther, H., Wienen, M., & Linz, H. 2014, A&A, 568, A41

Walmsley, C. M., Guesten, R., Angerhofer, P., Churchwell, E., & Mundy, L. 1986, A&A, 155, 129

Wilson, T. L., Ruf, K., Walmsley, C. M., Martin, R. N., Batrla, W., & Pauls, T. A. 1982, A&A, 115, 185

Yu, N. & Wang, J.-J. 2015, MNRAS, 451, 2507

Table 1 Emission lines observed as part of the MALT90 survey.

Emission lines	Frequency (GHz)	E_u/k [a] (K)	n_{crit} (cm^{-3})	Name	Detections[b]
Dense, 'low' E_u/k:					
HCO^+ (1–0)	89.188526	4.28	2×10^5	Formylium	3125 (87.9%)
HNC (1–0)	90.663572	4.35	3×10^5	Hydrogen Isocyanide	2993 (84.2%)
N_2H^+ (1–0)	93.173771	4.47	3×10^5	Diazenylium	2543 (71.5%)
HCN (1–0)	88.631847	4.25	3×10^6	Hydrogen Cyanide	2678 (75.3%)
Dense, 'low' E_u/k, optically thin:					
$H^{13}CO^+$ (1–0)	86.754330	4.16	2×10^5	Formylium, isotopologue	915 (25.7%)
$HN^{13}C$ (1–0)	87.090859	4.18	3×10^5	Hydrogen Isocyanide, isotopologue	547 (15.4%)
^{13}CS (2–1)	92.494303	6.66	3×10^5	Carbon monosulfide, isotopologue	171 (4.8%)
$^{13}C^{34}S$ (2–1)	90.926036	7.05	4×10^5	Carbon monosulfide, isotopologue	9 (0.3%)
Dense, 'high' E_u/k :					
$HC^{13}CCN$ (10–9)	90.593059	24.37	1×10^6	Cyanoacetylene, isotopologue	10 (0.3%)
HNCO 4(0,4)–3(0,3)	87.925238	10.55	1×10^6	Isocyanic Acid	296 (8.3%)
CH_3CN 5(1)–4(1)	91.985313	20.39	4×10^5	Methyl cyanide	103 (2.9%)
HC_3N (10–9)	90.978989	24.01	5×10^5	Cyanoacetylene	798 (22.4%)
HNCO 4(1,3)–3(1,2)	88.239027	53.86	6×10^6	Isocyanic Acid	0 (0.0%)
Dense, 'low' E_u/k, PDRs:					
C_2H (1–0) 3/2–1/2	87.316925	4.19	4×10^5	Ethynyl	1673 (47.0%)
Shocks:					
SiO (2–1)	86.847010	6.25	2×10^6	Silicon Monoxide	341 (9.6%)
Ionized gas:					
H 41α	92.034475			H-alpha	22 (0.6%)

[a]Excitation energies (E_u/k), Einstein A coefficients, and collisional rates were obtained from the Leiden Atomic and Molecular Database (LAMDA; Schöier et al. 2005) and Cologne Database for Molecular Spectroscopy (CDMS; Müller et al. 2001, 2005) assuming a gas temperature of 20 K. To derive critical densities, we used calculated collisional rates (γ) where possible and the equation $n_{crit} = A_u / \gamma$, where A_u is the Einstein A coefficient. For many of the more complex species, however, collisional rates have not been calculated. In these cases, we calculate an approximate critical density via $n_{crit} = A_u / (v\sigma)$, where v is the velocity of the molecule and σ is the collisional cross section which was assumed to be 10^{-15} cm^{-2}.
[b]These percentages are calculated with respect to the 3557 entries within the catalog

PASA (2016)
doi:10.1017/pas.2016.xxx

Table 2 An extract of the line emission toward the high-mass clumps covered by MALT90. See section 4 for a detailed description of its contents.

Clump	Dust peak			S	V_C	NL	τ	τ_{err}	HCO$^+$ (1–0)														
name	ℓ	b	flux						D	NG	T_A^*	$T_{A\,err}^*$	V_{LSR}	V_{err}	ΔV	ΔV_{err}	Π	Π_{err}	σ_{noise}	P_{fit}	Π_{SNR}	RA	HR
(1)	(2)	(3)	(4)	(5)	(6)	(7)	(8)	(9)	(10)	(11)	(12)	(13)	(14)	(15)	(16)	(17)	(18)	(19)	(20)	(21)	(22)	(23)	(24)
AGAL351.018+00.736_S	351.018	0.736	1.2	U	-2.91	4	0.00	0.00	Y	1	0.87	0.06	-2.61	0.16	4.79	0.37	4.32	0.35	0.27	0.121	12	1.2	0
AGAL351.021+00.566_S	351.021	0.566	1.71	P	-5.32	4	0.00	0.00	Y	1	0.65	0.03	-5.64	0.10	4.54	0.23	3.23	0.18	0.13	0.152	18	1.2	0
AGAL351.026−00.321_S	351.026	-0.321	1.02	A	-17.64	4	0.00	0.00	Y	1	0.20	0.03	-18.07	0.31	4.38	0.73	0.94	0.15	0.12	0.306	6	1.0	0
AGAL351.041−00.336_S	351.041	-0.336	0.47	A	-18.34	8	0.00	0.00	Y	1	1.65	0.04	-18.72	0.05	4.20	0.11	8.10	0.22	0.16	0.000	37	2.8	1
AGAL351.041+00.579_S	351.041	0.579	5.18	P	-5.73	4	0.00	0.00	Y	1	0.79	0.03	-5.75	0.08	3.93	0.18	3.39	0.17	0.13	0.002	20	2.1	1
AGAL351.131+00.771_S	351.131	0.771	0.51	Q	-5.43	6	0.00	0.00	Y	1	1.11	0.04	-5.37	0.08	4.63	0.19	5.53	0.23	0.18	0.798	24	1.2	0
AGAL351.139+00.756_S	351.139	0.756	1.48	Q	-5.56	8	0.69	0.28	Y	1	1.27	0.04	-5.65	0.07	4.55	0.16	6.66	0.27	0.18	0.937	24	1.0	0
AGAL351.141+00.776_S	351.141	0.776	1.37	U	-5.99	6	0.00	0.52	Y	1	0.92	0.04	-5.94	0.09	4.18	0.21	4.33	0.23	0.17	0.468	19	1.4	0
AGAL351.151+00.764_S	351.151	0.764	0.99	Q	-6.48	7	0.46	0.66	Y	1	0.86	0.04	-6.41	0.11	5.58	0.27	5.23	0.26	0.18	0.053	20	1.1	0
AGAL351.159+00.749_S	351.159	0.749	0.88	U	-6.96	6	0.93	0.70	Y	1	1.04	0.04	-6.64	0.10	5.68	0.23	6.58	0.27	0.18	0.110	24	1.9	1
AGAL351.161+00.697_S	351.161	0.697	1.49	A	-5.81	9	0.27	0.31	Y	1	3.54	0.03	-5.80	0.02	5.77	0.05	23.86	0.26	0.13	0.000	91	3.8	1
AGAL351.173+00.632_S	351.173	0.632	23.78	U	-5.24	9	0.22	0.09	Y	1	1.78	0.02	-5.38	0.04	5.95	0.09	11.57	0.20	0.12	0.003	58	2.3	1
AGAL351.173+00.661_S	351.173	0.661	3.74	U	-3.22	7	0.86	0.25	Y	2	3.07	0.04	-3.62	0.01	4.11	0.04	10.83	0.26	0.12	0.000	41	1.9	1
AGAL351.178+00.729_S	351.178	0.729	1.35	P	-6.86	4	0.00	0.00	Y	1	0.79	0.03	-6.93	0.12	6.71	0.28	5.55	0.23	0.15	0.004	25	2.3	1
AGAL351.184+00.577_S	351.184	0.577	0.59	U	-4.78	7	0.00	0.16	Y	1	2.82	0.03	-4.61	0.02	3.86	0.04	12.33	0.17	0.12	0.000	72	3.8	1
AGAL351.219+00.672_S	351.219	0.672	1.2	U	-4.06	9	0.04	0.22	Y	1	3.64	0.04	-4.17	0.01	3.08	0.04	12.71	0.22	0.14	0.000	58	2.1	1
AGAL351.228+00.691_S	351.228	0.691	2.79	A	-4.22	9	0.39	0.16	Y	1	3.36	0.03	-4.21	0.02	3.58	0.04	13.75	0.19	0.12	0.000	71	2.9	1
AGAL351.236+00.651_S	351.236	0.651	5.48	C	-1.82	9	0.00	0.00	Y	1	4.35	0.04	-1.85	0.01	3.70	0.03	18.07	0.22	0.14	0.000	83	3.3	1
AGAL351.244+00.669_S	351.244	0.669	4.38	C	-2.83	11	0.04	0.28	Y	2	5.67	0.03	-3.06	0.01	5.48	0.03	30.75	0.31	0.15	0.000	100	2.0	1
AGAL351.251+00.652_S	351.251	0.652	20.46	A	-0.42	10	0.43	0.15	Y	1	4.12	0.03	-0.78	0.02	4.48	0.04	20.59	0.20	0.13	0.000	103	3.7	1
AGAL351.289+00.664_S	351.289	0.664	11.44	Q	-2.03	9	0.32	0.31	Y	2	2.69	0.03	-2.38	0.02	4.84	0.05	12.61	0.25	0.13	0.002	51	1.4	1
AGAL351.308+00.684_S	351.308	0.684	3.13	U	-3.75	4	0.00	0.00	Y	1	1.10	0.03	-3.81	0.06	4.46	0.14	5.34	0.18	0.13	0.217	29	1.4	0
AGAL351.353+00.696_S	351.353	0.696	0.78	U	-1.61	5	1.76	0.84	Y	1	1.64	0.07	-1.79	0.08	3.91	0.20	8.86	0.47	0.29	0.000	19	2.0	1
AGAL351.359+00.706_S	351.359	0.706	1.12	P	-1.97	6	0.00	0.00	Y	1	1.62	0.03	-2.06	0.04	4.62	0.10	8.15	0.20	0.14	0.000	40	3.4	1
AGAL351.361+00.664_S	351.361	0.664	0.81	P	-2.88	9	0.99	0.37	Y	1	3.66	0.04	-2.88	0.03	5.06	0.06	20.12	0.28	0.18	0.000	73	3.7	1
AGAL351.378+00.706_S	351.378	0.706	4.58	P	-4.53	6	0.13	0.37	Y	1	2.48	0.03	-4.31	0.03	4.75	0.07	12.62	0.21	0.14	0.000	61	5.0	1
AGAL351.383−00.181_S	351.383	-0.181	2.82	H	-66.05	4	0.00	0.00	Y	1	0.36	0.04	-65.63	0.15	2.91	0.36	1.17	0.18	0.14	0.319	6	0.9	0
AGAL351.386+00.667_S	351.386	0.667	0.88	Q	-2.82	9	0.56	0.13	Y	2	3.63	0.04	-3.44	0.03	6.28	0.06	23.42	0.32	0.17	0.000	73	2.3	1
AGAL351.403+00.659_S	351.403	0.659	6.73	P	-5.59	9	0.06	0.31	Y	1	3.14	0.03	-5.67	0.04	8.66	0.11	28.45	0.34	0.20	0.000	83	3.2	1
AGAL351.406+00.557_S	351.406	0.557	3.46	U	-4.96	4	0.00	0.00	Y	1	1.27	0.04	-4.94	0.08	4.61	0.18	6.43	0.28	0.20	0.423	23	1.5	1
AGAL351.408+00.634_S	351.408	0.634	0.54	U	-6.94	9	0.17	0.22	Y	2	3.74	0.03	-6.22	0.03	8.11	0.07	32.00	0.38	0.19	0.000	84	4.3	1
AGAL351.409+00.567_S	351.409	0.567	2.38	U	-5.07	4	0.00	0.00	Y	1	1.50	0.04	-5.00	0.07	5.18	0.16	8.48	0.29	0.19	0.034	29	1.9	1
AGAL351.414+00.594_S	351.414	0.594	0.75	U	-4.74	5	0.00	0.00	Y	1	1.76	0.04	-4.69	0.06	5.30	0.15	10.04	0.31	0.21	0.000	32	2.7	1
AGAL351.416+00.646_S	351.416	0.646	0.52	A	-7.95	11	0.29	0.10	Y	1	6.68	0.04	-7.93	0.02	6.21	0.04	48.31	0.42	0.21	0.000	116	5.5	1
AGAL351.421+00.551_S	351.421	0.551	59.26	U	-4.68	5	0.00	0.00	Y	1	1.08	0.04	-4.72	0.10	5.89	0.23	7.03	0.27	0.19	0.222	26	1.2	0
AGAL351.431+00.649_S	351.431	0.649	0.44	U	-5.39	10	0.41	0.10	Y	2	4.52	0.04	-5.39	0.03	6.50	0.06	30.91	0.45	0.21	0.001	69	1.5	1
AGAL351.434+00.676_S	351.434	0.676	9.11	U	-3.88	12	0.64	0.06	Y	1	2.58	0.03	-4.58	0.04	7.10	0.08	19.92	0.26	0.14	0.000	76	2.6	1
AGAL351.444+00.659_S	351.444	0.659	8.41	A	-4.67	13	1.30	0.03	Y	1	4.68	0.02	-4.81	0.02	8.06	0.04	42.94	0.30	0.14	0.000	142	6.9	1
AGAL351.456+00.666_S	351.456	0.666	40.8	U	-4.52	12	0.82	0.04	Y	1	3.44	0.02	-4.75	0.02	7.24	0.06	27.84	0.25	0.13	0.000	110	3.5	1
AGAL351.461+00.644_S	351.461	0.644	10.05	U	-4.29	12	0.48	0.06	Y	1	2.27	0.03	-4.48	0.04	7.01	0.09	17.02	0.22	0.14	0.000	77	3.9	1
AGAL351.464−00.461_S	351.464	-0.461	2.73	H	-21.74	2	0.00	0.00	Y	2	0.23	0.42	-21.07	4.64	5.26	0.26	0.84	0.20	0.18	0.676	4	1.0	0
AGAL351.466+00.591_S	351.466	0.591	1.55	U	-3.84	7	0.00	0.00	Y	1	0.96	0.04	-4.27	0.12	6.24	0.29	6.35	0.27	0.20	0.000	23	2.2	1
AGAL351.466+00.682_S	351.466	0.682	0.85	U	-4.25	10	0.75	0.09	Y	1	2.43	0.04	-4.39	0.06	7.29	0.14	18.62	0.37	0.23	0.000	50	2.7	1
AGAL351.469+00.672_S	351.469	0.672	8.9	U	-4.37	10	0.53	0.09	Y	1	2.86	0.04	-4.72	0.04	6.42	0.10	19.74	0.33	0.21	0.000	60	2.4	1
AGAL351.476−00.452_S	351.476	-0.452	2.71	H	-22.00	2	0.27	1.53	Y	1	0.18	0.04	-25.48	0.43	3.36	1.02	0.80	0.18	0.17	0.307	4	1.1	0
AGAL351.479−00.464_S	351.479	-0.464	1.02	H	-21.52	1	0.00	0.00	N	-1	0.00	0.00	0.00	0.00	0.00	0.00	0.00	0.00	0.00	0.000	0	0.0	0
AGAL351.491+00.691_S	351.491	0.691	0.58	U	-2.64	10	0.19	0.08	Y	1	2.16	0.03	-2.52	0.04	6.95	0.10	16.35	0.24	0.14	0.000	67	4.1	1
AGAL351.496+00.691_S	351.496	0.691	3.59	A	-2.87	8	0.21	0.07	Y	1	2.04	0.03	-2.66	0.04	6.72	0.09	15.01	0.23	0.13	0.000	66	4.7	1
AGAL351.498+00.646_S	351.498	0.646	3.06	U	-3.94	7	0.04	0.19	Y	1	1.76	0.03	-4.41	0.05	5.34	0.12	9.74	0.26	0.16	0.000	38	2.6	1
AGAL351.526+00.707_S	351.526	0.707	1.47	A	-2.73	8	0.38	0.11	Y	1	1.28	0.02	-2.77	0.05	5.76	0.12	7.97	0.18	0.12	0.000	45	2.4	1
AGAL351.529−00.556_S	351.529	-0.556	1.51	A	-21.80	7	0.68	0.23	Y	1	0.37	0.03	-20.56	0.17	3.66	0.41	1.48	0.17	0.14	0.241	9	1.3	0
AGAL351.533−00.574_S	351.533	-0.574	1.22	U	-21.67	5	0.00	0.00	Y	1	0.43	0.04	-21.13	0.13	2.82	0.31	1.65	0.20	0.14	0.299	8	1.0	0
AGAL351.548+00.186_S	351.548	0.186	0.6	P	-40.50	6	0.00	0.00	Y	1	0.91	0.02	-40.60	0.08	6.21	0.18	6.30	0.19	0.12	0.971	33	1.1	0

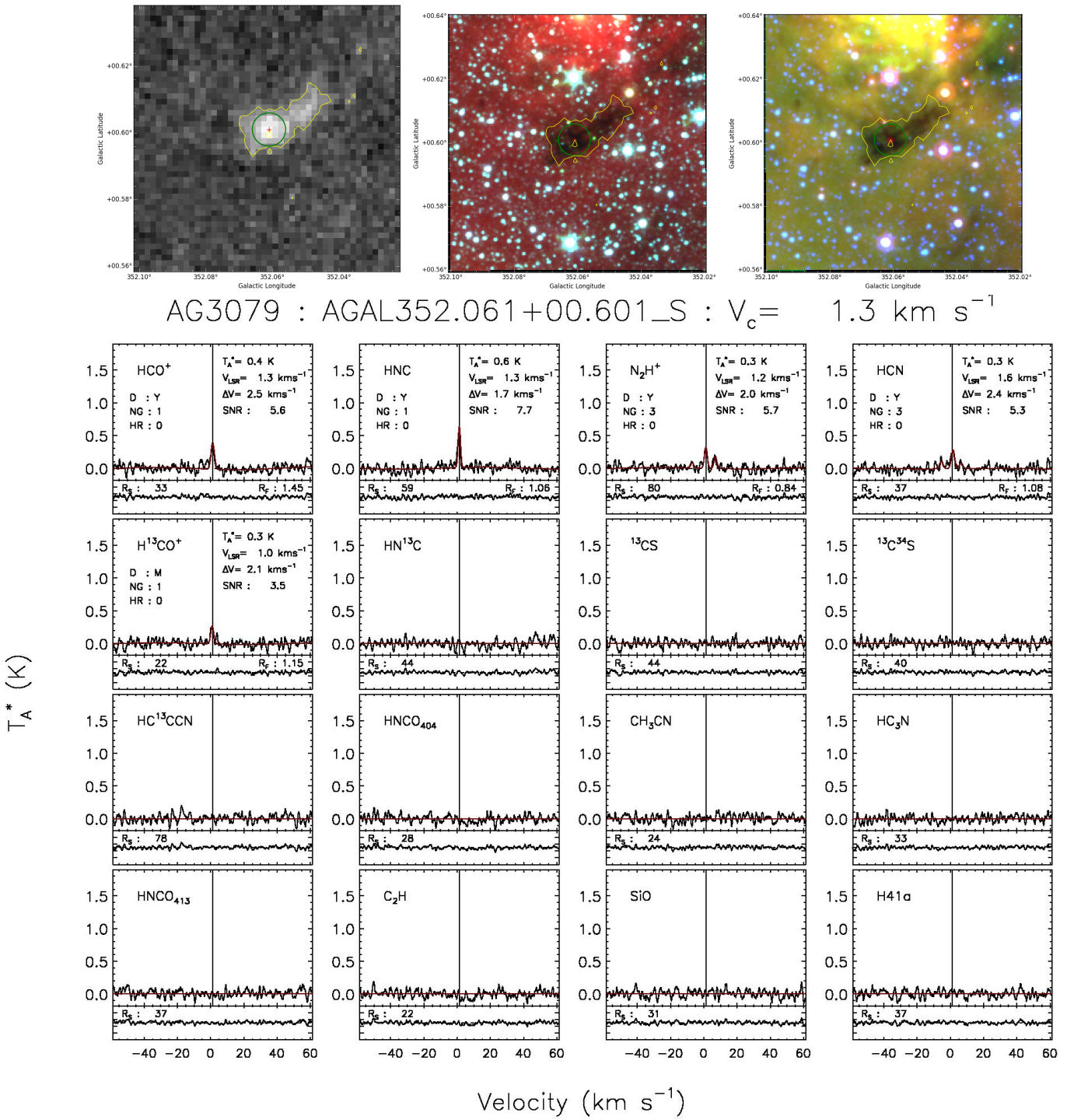

Figure 1. ATLASGAL/*Spitzer* images and MALT90 spectra toward AGAL352.061+00.601_S : an example of a 'quiescent' clump. *Upper images (from left to right):* ATLASGAL 870 μm dust continuum emission in grey-scale, *Spitzer* 3–8 μm three colour image (3.6 μm in blue, 4.5 μm in green, and 8.0 μm in red), and *Spitzer* 3–24 μm three colour image (3.6 μm in blue, 8.0 μm in green, and 24 μm in red). In all images yellow contours show the 870 μm dust continuum emission. The red cross marks the peak of the ATLASGAL dust clump toward which the MALT90 spectra were extracted (any other ATLASGAL clumps located nearby are marked as blue crosses; they are listed as separate entries in the MALT90 catalog). The green circle shows the angular resolution of the MALT90 data (∼38"). *Lower panels:* MALT90 spectra extracted toward this ATLASGAL clump. The panels show the individual spectra (black) overlaid with the best-fit profile (red; which includes any additional baseline component). If emission was detected, the derived parameters from the best-fit Gaussian profile are labelled. The consensus velocity is labelled and shown in all panels as the solid vertical line. Under each panel, the residual spectrum is displayed with labels showing the residual in the complete spectrum (R_s) and the residual in the fit range (R_f).

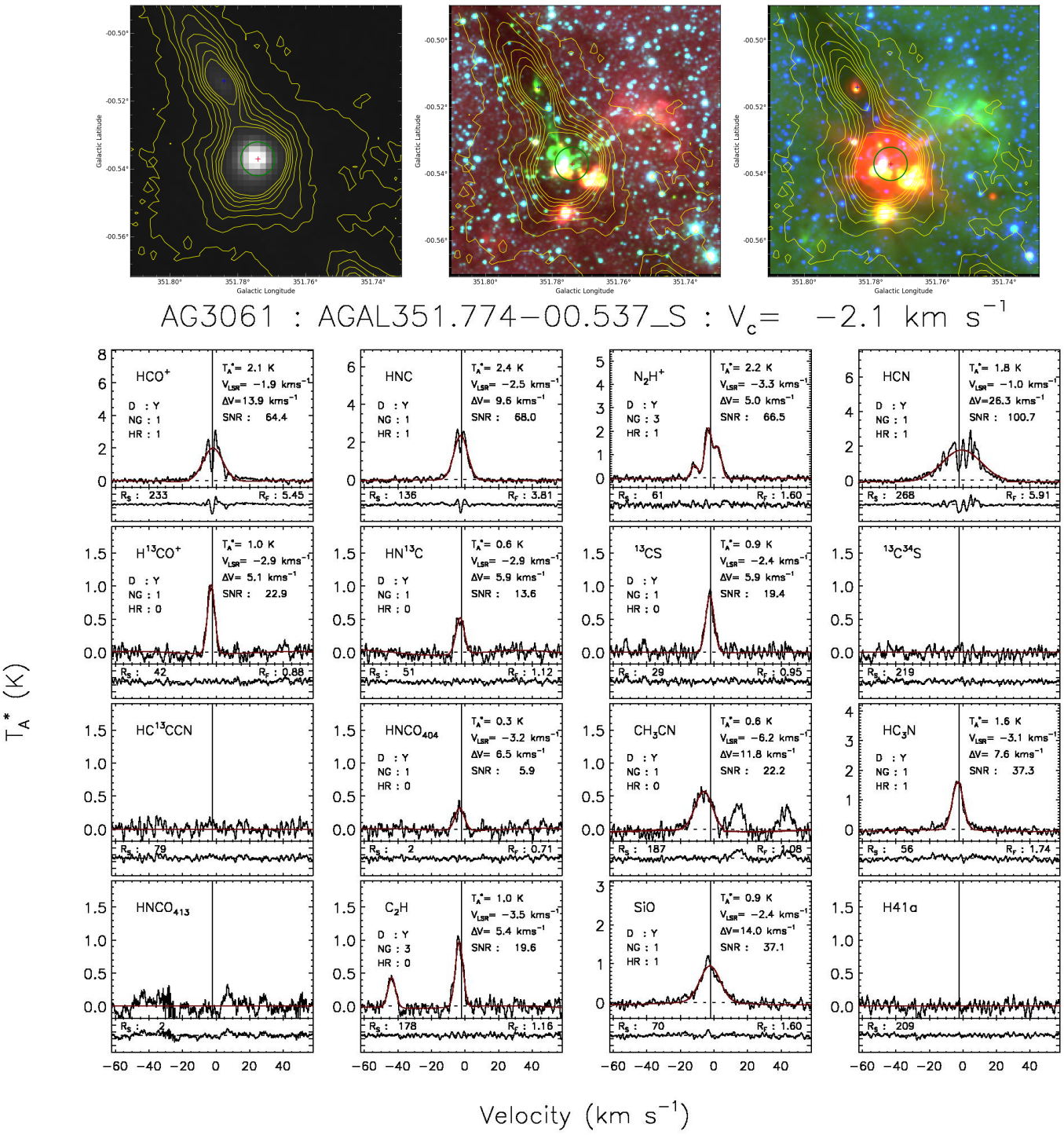

Figure 2. ATLASGAL/*Spitzer* images and MALT90 spectra toward AGAL351.774-00.537_S: an example of a 'protostellar' clump associated with bright and extended 'green' (4.5 μm) emission, indicative of shocked gas. The images and spectra are the same as plotted and described in Fig. 1.

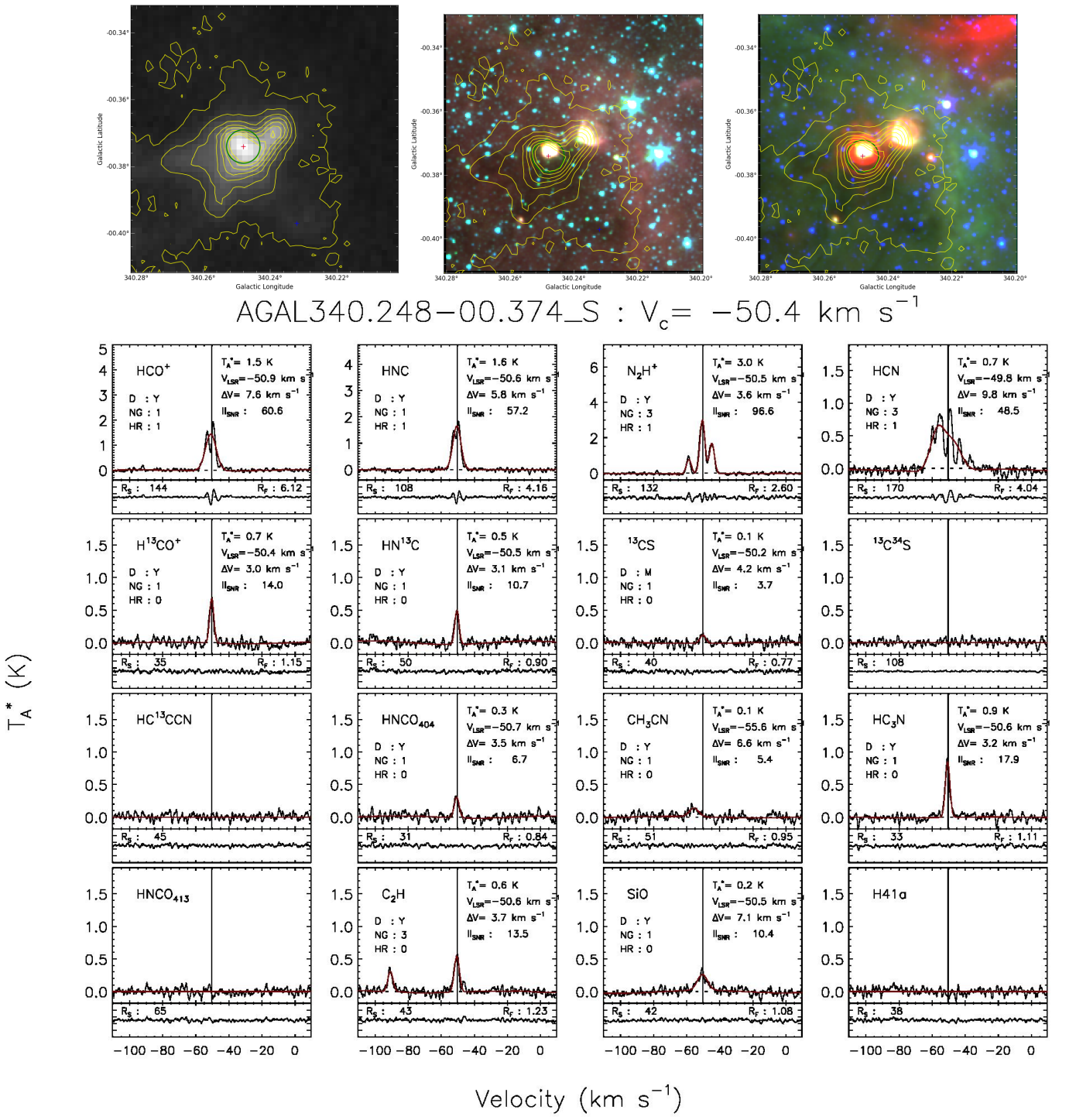

Figure 3. ATLASGAL/*Spitzer* images and MALT90 spectra toward AGAL340.248-00.374_S: an example of a 'HII' region. The images and spectra are the same as plotted and described in Fig. 1.

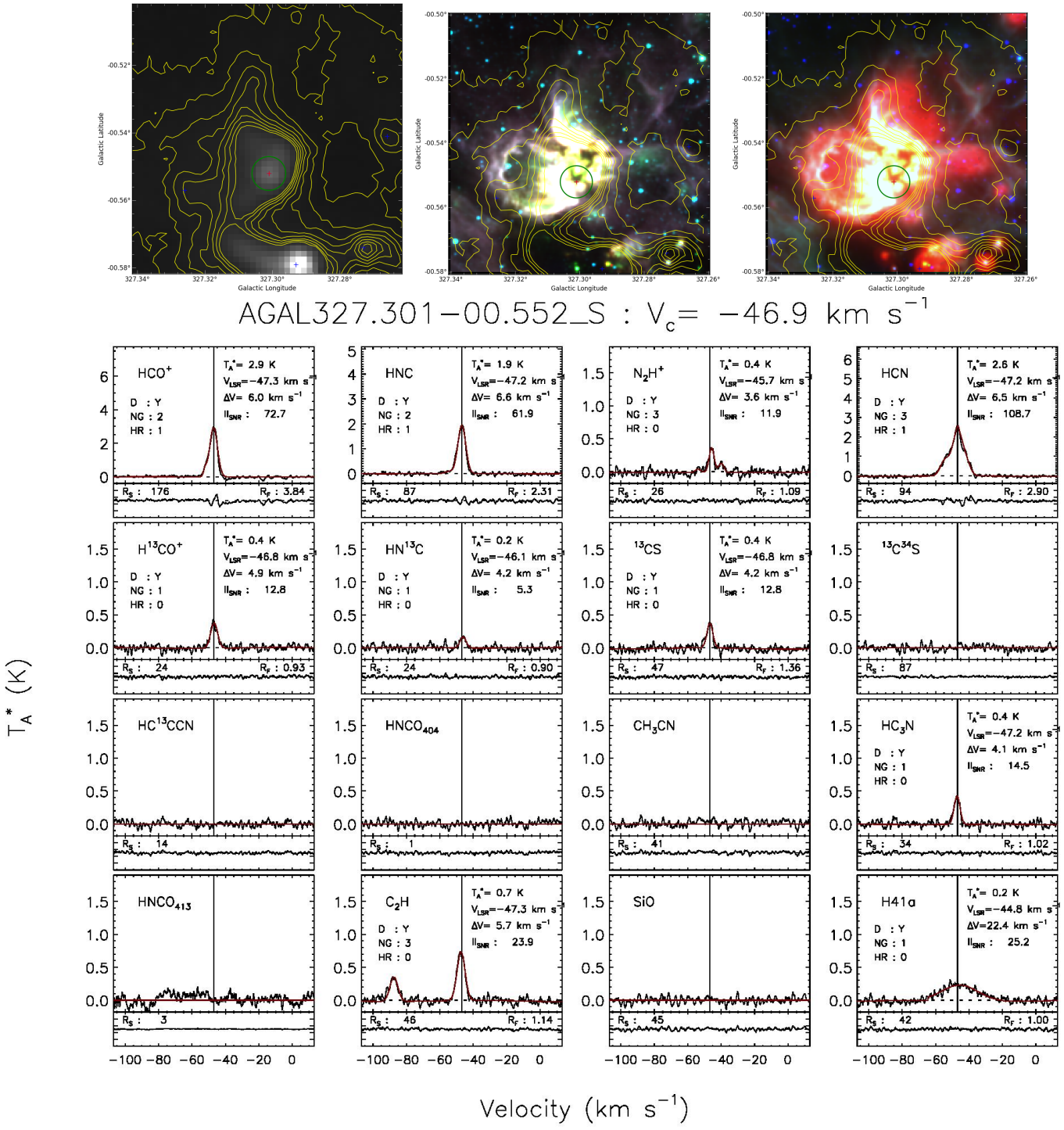

Figure 4. ATLASGAL/*Spitzer* images and MALT90 spectra toward AGAL327.301-00.552_S: an example of a 'HII' region, with a clear detection of H 41α emission. The images and spectra are the same as plotted and described in Fig. 1.

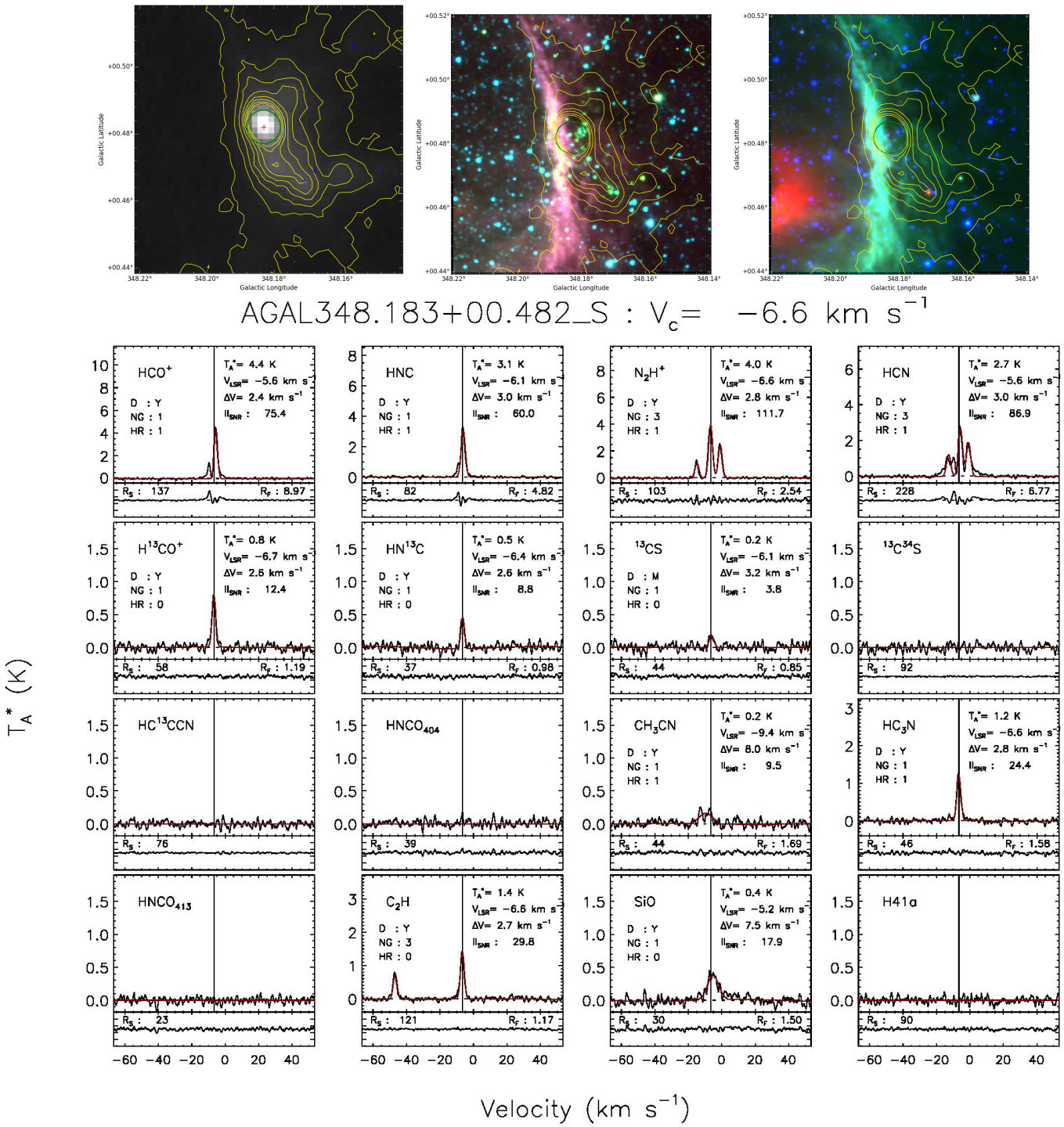

Figure 5. ATLASGAL/*Spitzer* images and MALT90 spectra toward AGAL348.183+00.482_S : an example of a 'PDR' clump. The images and spectra are the same as plotted and described in Fig. 1.

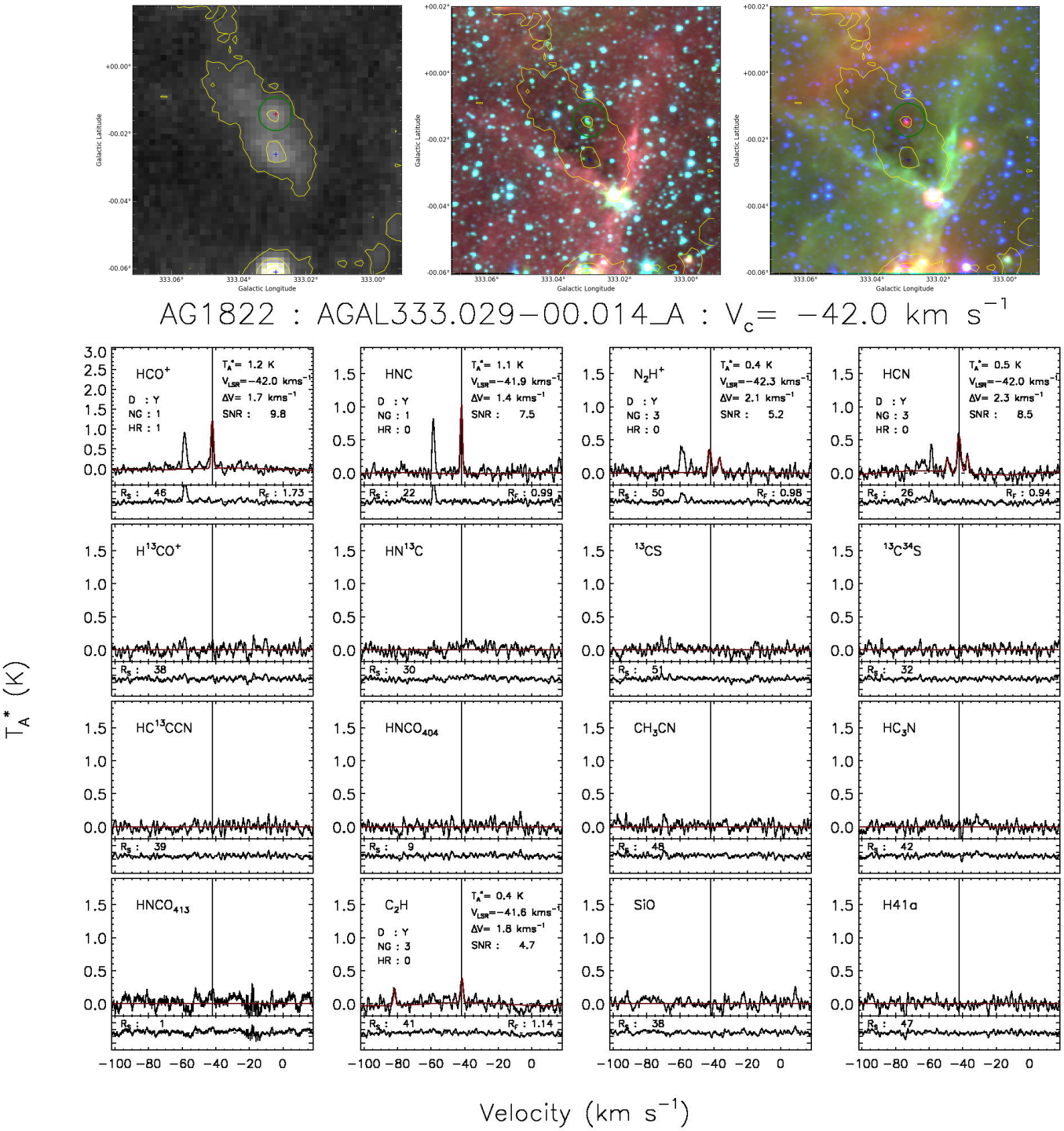

Figure 6. ATLASGAL/*Spitzer* images and MALT90 spectra toward AGAL333.029-00.014_A : an example of a 'Protostellar' clump with two velocity components detected along the line of sight (component A is shown here, component B is shown in figure 7). The images and spectra are the same as plotted and described in Fig. 1.

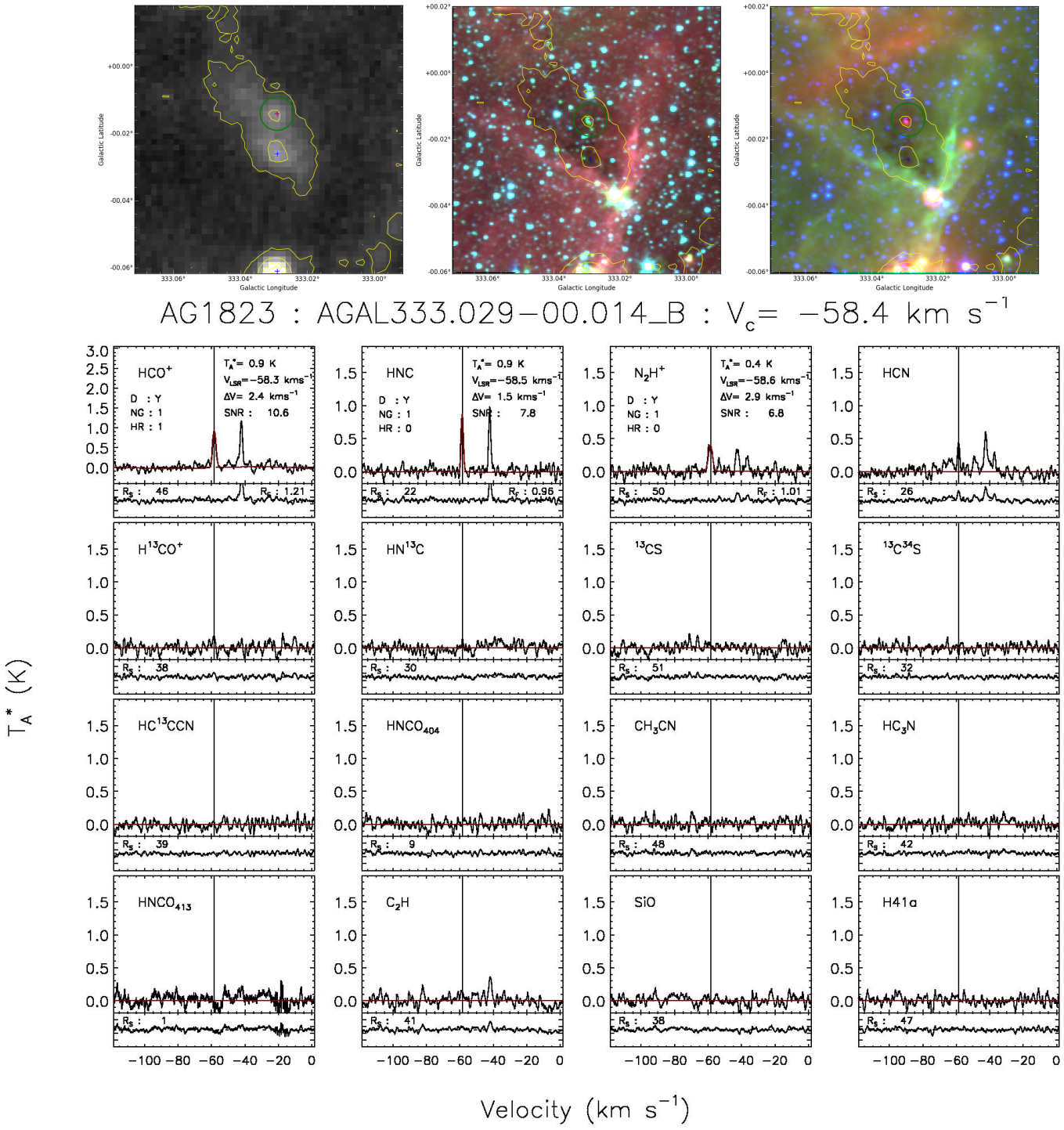

Figure 7. ATLASGAL/*Spitzer* images and MALT90 spectra toward AGAL333.029-00.014_B : an example of a 'Protostellar' clump with two velocity components detected along the line of sight (component B is shown here, component A is shown in figure 6). The images and spectra are the same as plotted and described in Fig. 1.

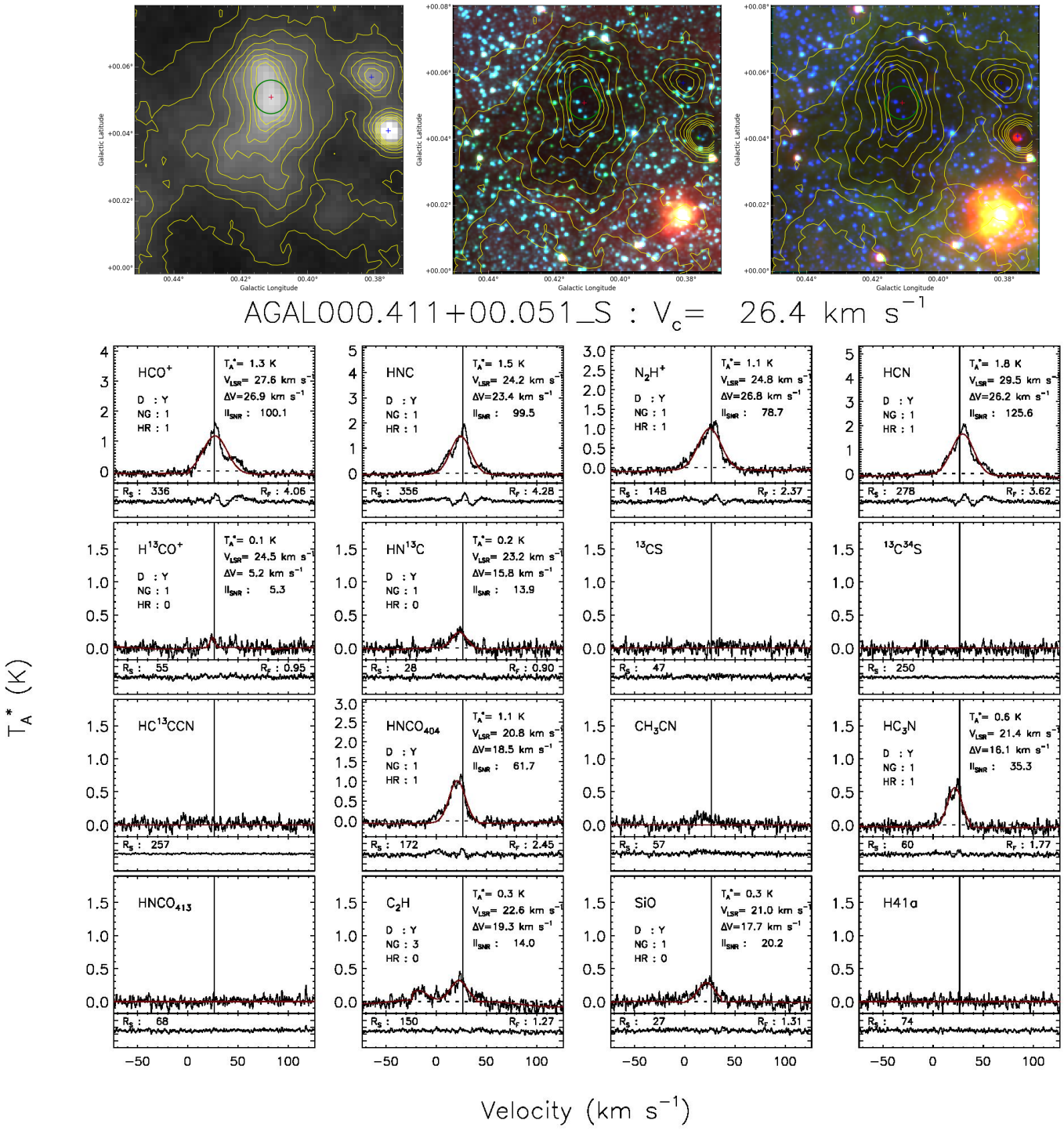

Figure 8. ATLASGAL/*Spitzer* images and MALT90 spectra toward AGAL000.411+00.051_S: an example of a clump located in the Central Molecular Zone (note the broad line-widths). The images and spectra are the same as plotted and described in Fig. 1.

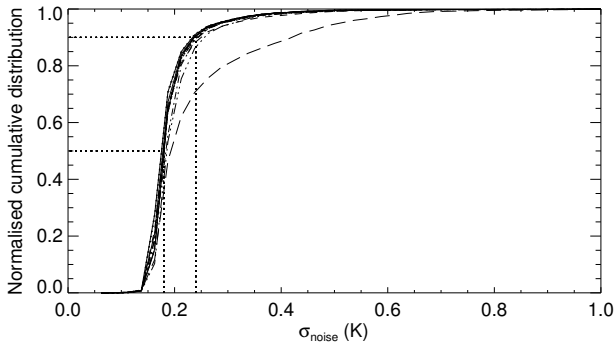

Figure 9. Normalized cumulative distributions of σ_{noise} derived from the spectra of each emission line. The bold line shows the cumulative distribution for the synthetic spectra (see section 3.5). The tail at high noise levels arises from spectra near the map edges and those obtained when the weather was variable. The noise distribution derived from the spectra of each of the 16 lines follow each other closely, with the exception of HNCO 4(1,3)–3(1,2) which suffered from serious band distortions (marked with the dashed line). For all other lines, 90% of the spectra have $\sigma_{noise} < 0.24$ K and 50% have $\sigma_{noise} < 0.18$ K (these σ_{noise} levels are marked with the dotted lines).

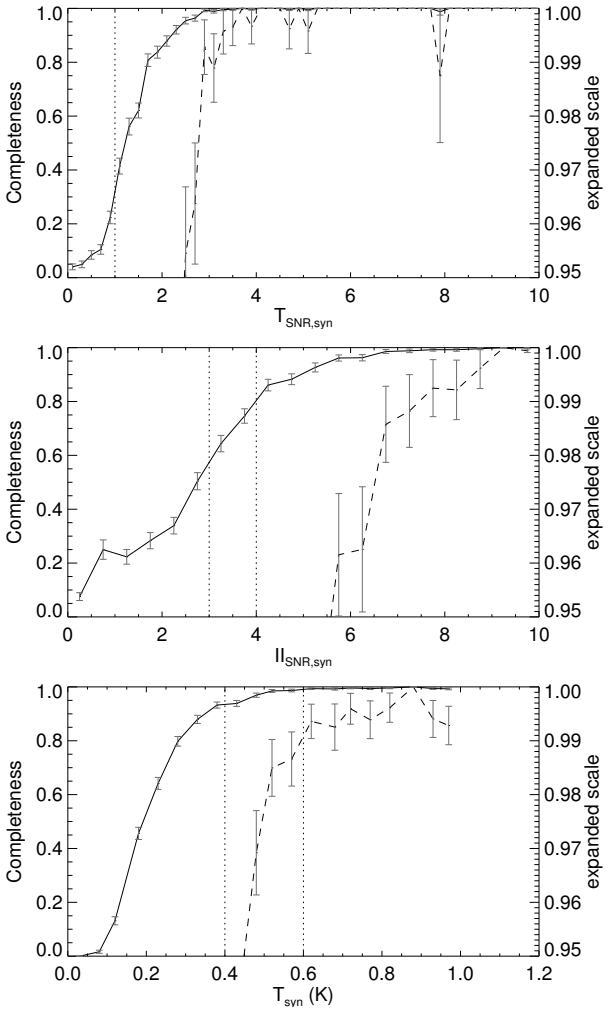

Figure 10. Completeness (fraction of sources detected) as a function of the $T_{SNR,syn}$ (upper panel), $II_{SNR,syn}$ (middle panel), and input T_{syn} (lower panel). In all panels the dashed curves correspond to the expanded scale shown on the right axis. The error bars show the statistical uncertainties in the synthetic sample. The vertical dotted lines in the upper and middle panels mark the selection criteria imposed for detections to be included within the catalog (i.e., $T_{SNR} > 1$ and $II_{SNR} > 3$ or > 4, for 'marginal' and 'reliable' detections, respectively). The vertical dotted lines in the lower panel mark the completeness levels. The achieved completeness levels are >95% for detections with a measured T_A^* > 0.4 K and > 99% for detections with a T_A^* > 0.6 K.

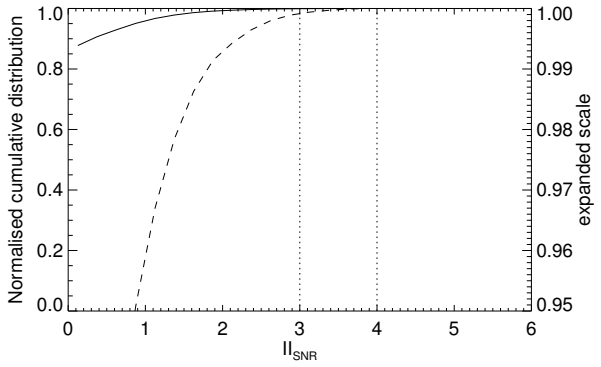

Figure 11. Normalized cumulative distributions in II_{SNR} for the synthetic noise spectra (note, this will characterise accidental detections due to noise and baseline fluctuations). The dashed curves correspond to the expanded scale shown on the right axis. The vertical dotted lines mark the selection criteria imposed for detections to be included within the catalog: an II_{SNR} of > 3 for 'marginal' and > 4 for 'reliable' detections, respectively. We find that the probability of a false-positive detection is $< 0.3\%$ for an $II_{SNR} > 3$.

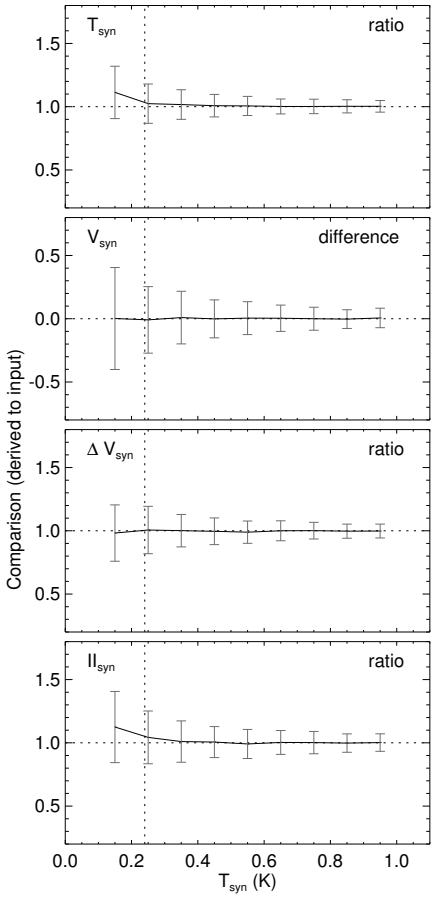

Figure 12. Reliability with which the derived parameters (amplitude, velocity, line-width, and integrated intensity, upper to lower panels respectively) are estimated. These reliabilities were determined by comparing the fitting results with the known characteristics used to generate the synthetic profiles (these comparisons are shown as ratios, with the exception of velocity, which are differences). The error bars reflect the uncertainty with which the automated routine estimates their values. The dotted vertical lines mark a T_{syn} of 0.24 K (90% of the spectra have noise less than this value).

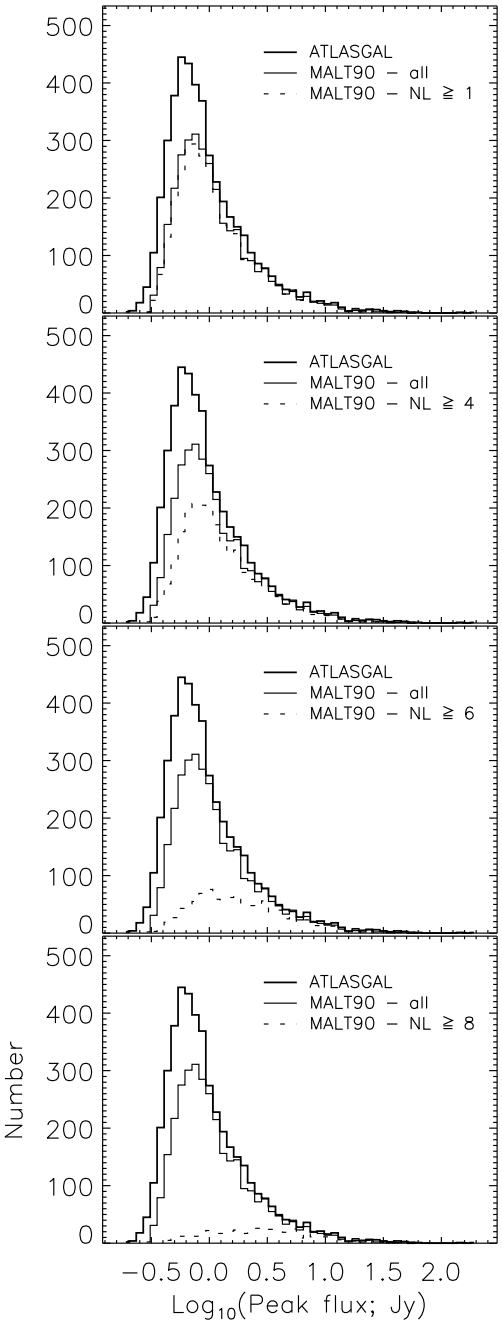

Figure 13. Histograms of the 870 μm peak flux for clumps covered by the MALT90 survey (thin histogram). In all panels clumps from the ATLASGAL survey are shown as thick histograms, while the dotted histograms show the flux distribution of those clumps covered by MALT90 survey and detected in more than the labeled number of lines (i.e. NL $\geq$ 1, 4, 6 and 8; upper to lower panels, respectively).

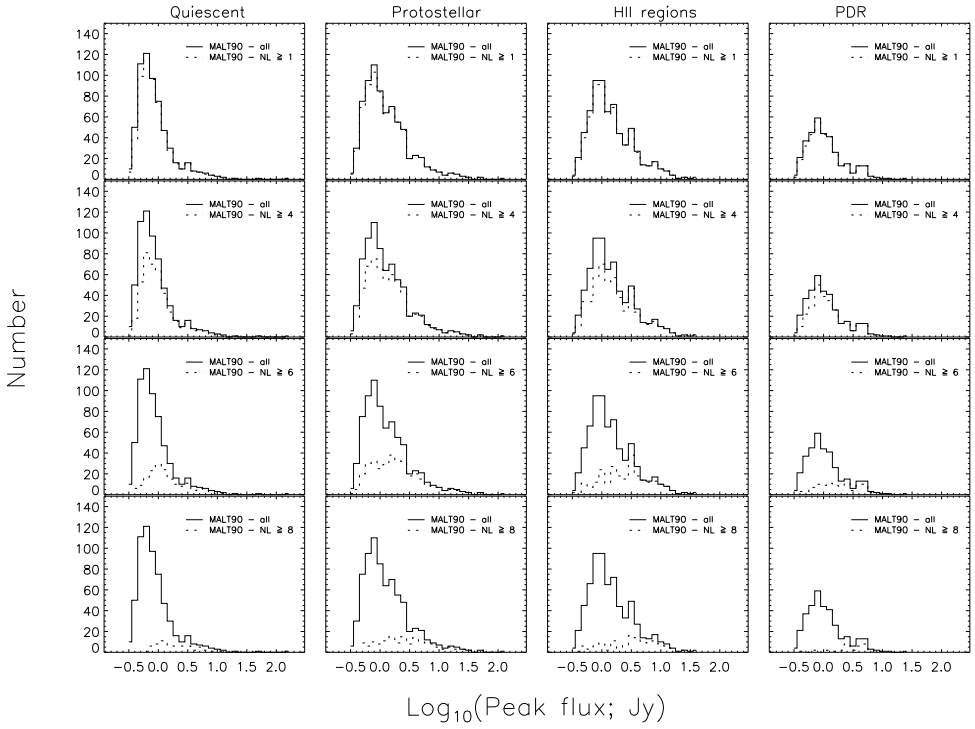

Figure 14. Histograms of the 870 μm peak flux for clumps covered by the MALT90 survey, separated by the IR-based categories (quiescent, prototstellar, H II regions, and PDRs, left to right, respectively). In all panels clumps included within MALT90 are shown as thin histograms, while the dotted histograms show the flux distribution of those clumps covered by MALT90 survey and detected in more than the labeled number of lines (i.e. NL $\geq$ 1, 4, 6 and 8; upper to lower panels, respectively).

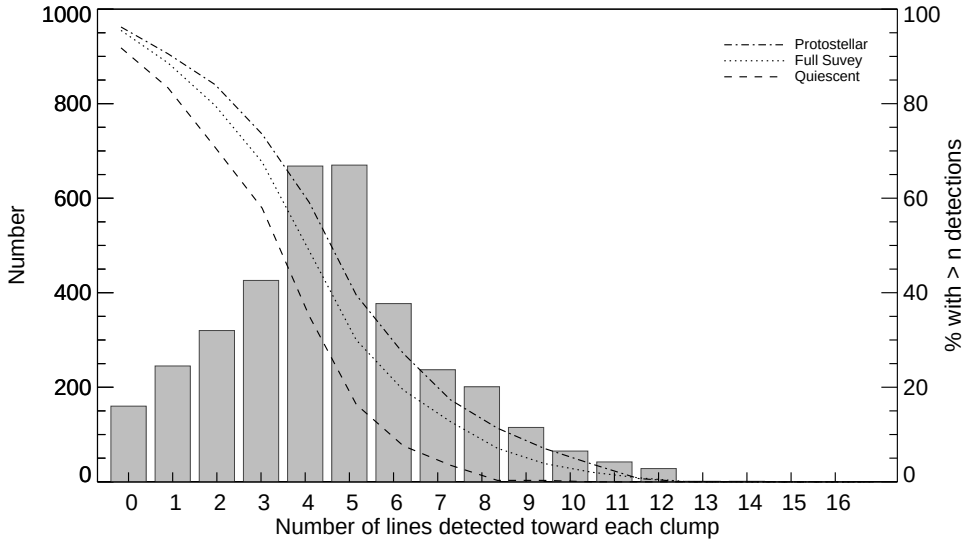

Figure 15. Number of clumps plotted as a function of the number of emission lines detected toward each (bar plot; left axis). The dotted line (right axis) shows the percentage of clumps with > n detections in the full survey. Most clumps ($\sim$ 96%) are detected in one or more of the dense gas tracers, $\sim$ 48% of the clumps have detections from 4 or more emission lines, while two clumps are detected in 13 or more lines. Also overlaid are the percentages of quiescent and protostellar clumps with > n detections (right axis; dashed and dot-dashed lines respectively). Clumps with active star formation (indicated by the 'protostellar' curve) have a both a higher percentage of detections and more lines detected towards them compared to the full survey and those clumps that appear to be more quiescent.

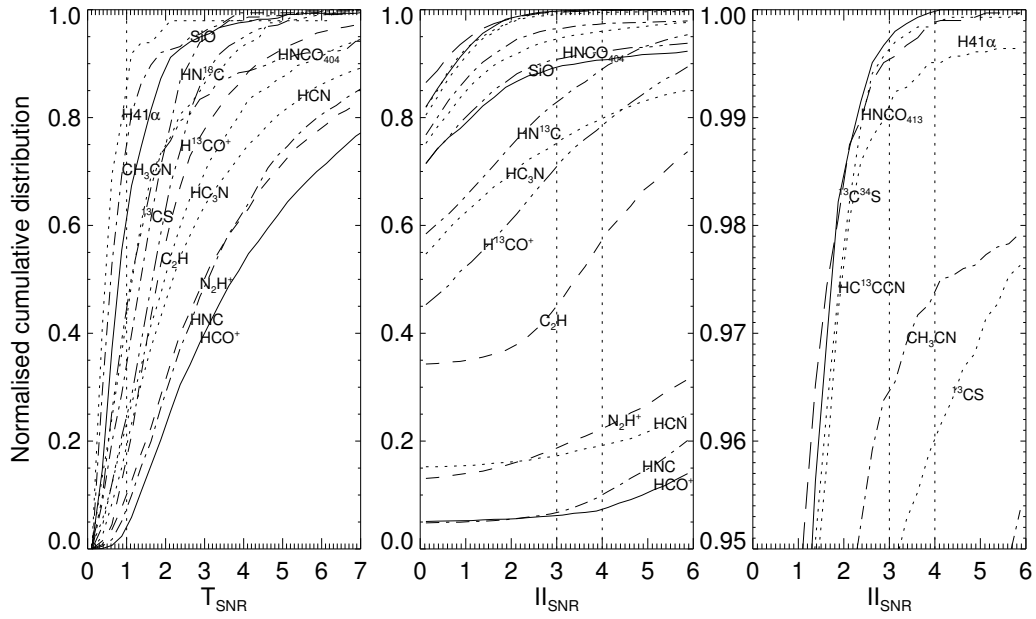

Figure 16. Normalized cumulative distributions of T_{SNR} (left panel) and II_{SNR} (middle and right panels). In all panels curves are labelled with the name of corresponding emission line. The vertical dotted lines mark the selection criteria imposed for detections to be included within the catalog: $T_{SNR} > 1$ and an $II_{SNR} > 3$ for 'marginal' or > 4 for 'reliable' detections, respectively. Flat curves imply that the inclusion/exclusion of detections is insensitive to the exact choice of the selection criteria (i.e., in the II_{SNR} plot for HCO^+, HNC, N_2H^+, HCN, SiO, HNCO, CH_3CN, and H 41α). In contrast, for curves that rise steeply, the exact choice of the II_{SNR} (3 or 4) does significantly affect the number of reported detections included in the catalog (i.e., for C_2H, $H^{13}CO^+$, HC_3N, $HN^{13}C$, and ^{13}CS).

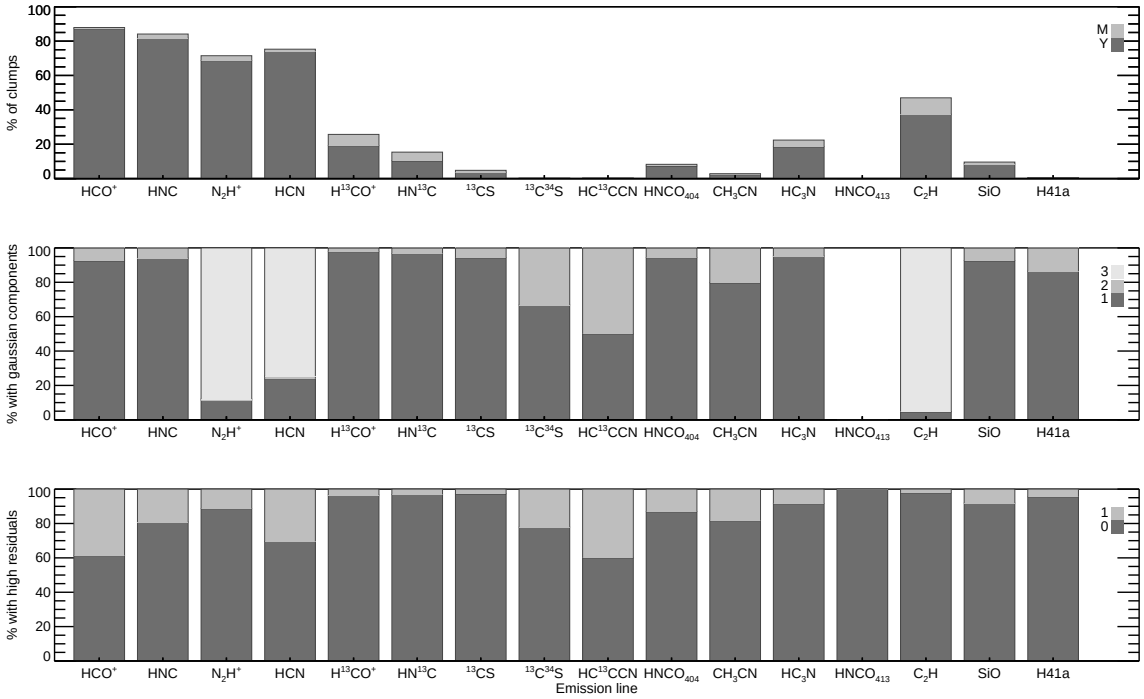

Figure 17. Detection rates (upper panel; separated by the significance of the detection, 'Y' or 'M'), the number of Gaussian profiles in the best-fit for these detections (middle panel; 1, 2, or 3), and the significance of the residuals in the fit range (lower panel; R_f <1.5, HR = 0 or $R_f > 1.5$, HR = 1) for all emission lines. Note for HNCO 4(1,3)–3(1,2), since there was no emission detected toward any of the clumps, the percentages in the top two panels are zero, however, the lower panel (which plots the residual in the fit range) shows that all the spectra have low residuals, which is consistent with non detections in all cases.

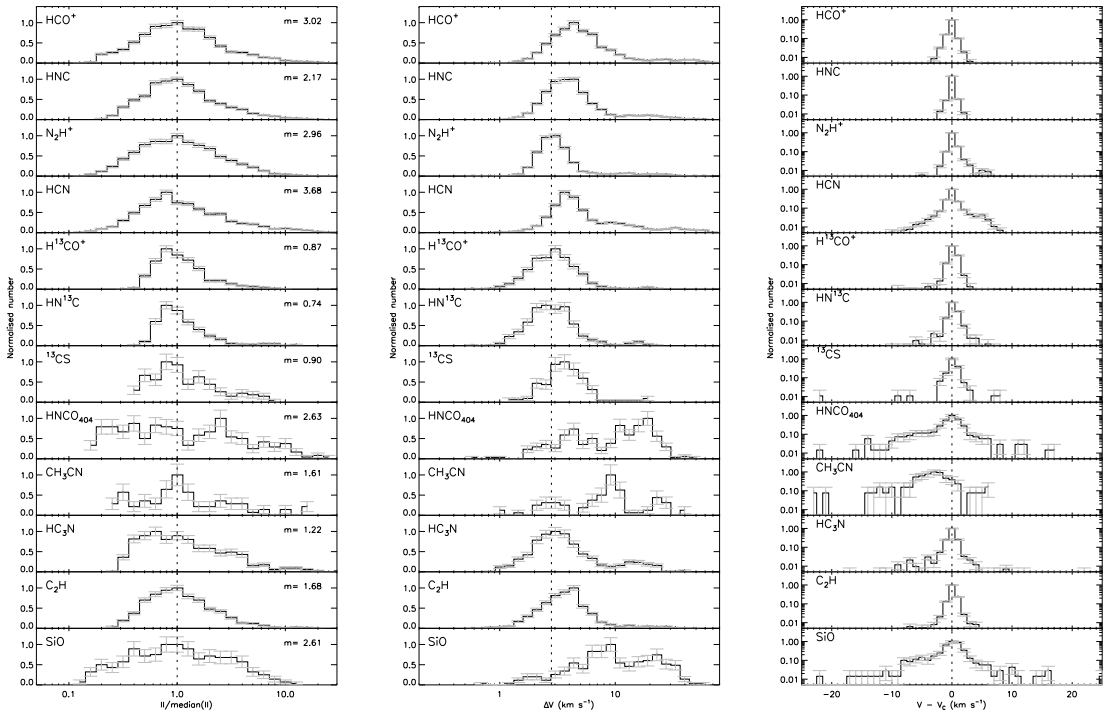

Figure 18. Histograms of the integrated intensity (II, relative to the median, *left*), line width (ΔV, *middle*), and V-V_C (*right*) for most of the emission lines (we only include in these plots those emission lines with more than 50 detections within the survey, see Table 1). The vertical dotted lines mark a value of 1.0 for the ratio of II to median(II), a line-width of 2.8 km s^{-1}, (the mean value derived from N_2H^+), and a value of 0 for the velocity difference (V-V_C), respectively. They are included for ease of comparison between the panels. Note that the y-axes for the right column are in a logarithmic scale. The error bars show the $\sqrt{N}$ uncertainties.

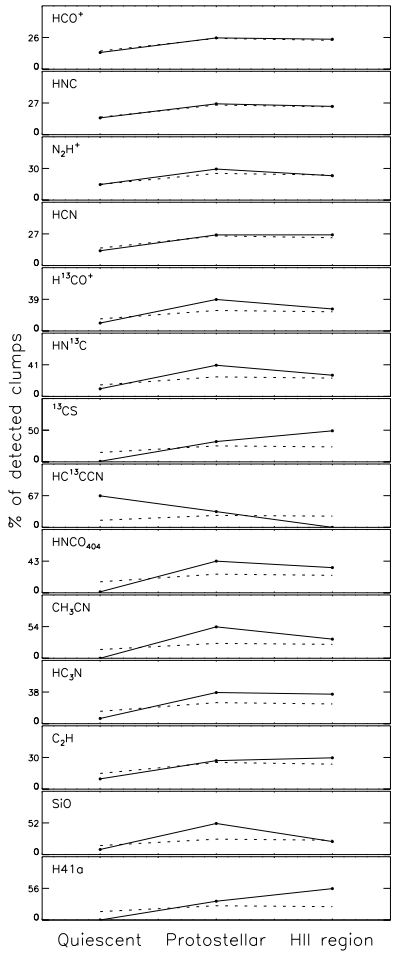

Figure 19. Detection rates for most emission lines as a function of IR-based category (HNCO 4(1,3)–3(1,2) and $^{13}C^{34}S$ were not plotted here since they had 0 and 9 detections within the survey, respectively) for clumps located outside of the CMZ (i.e., ± 10 degrees of the Galactic Centre). The dotted line in all panels shows the percentage of clumps detected from the survey as a whole within each of the classifications (19%, 22%, and 21%, respectively).

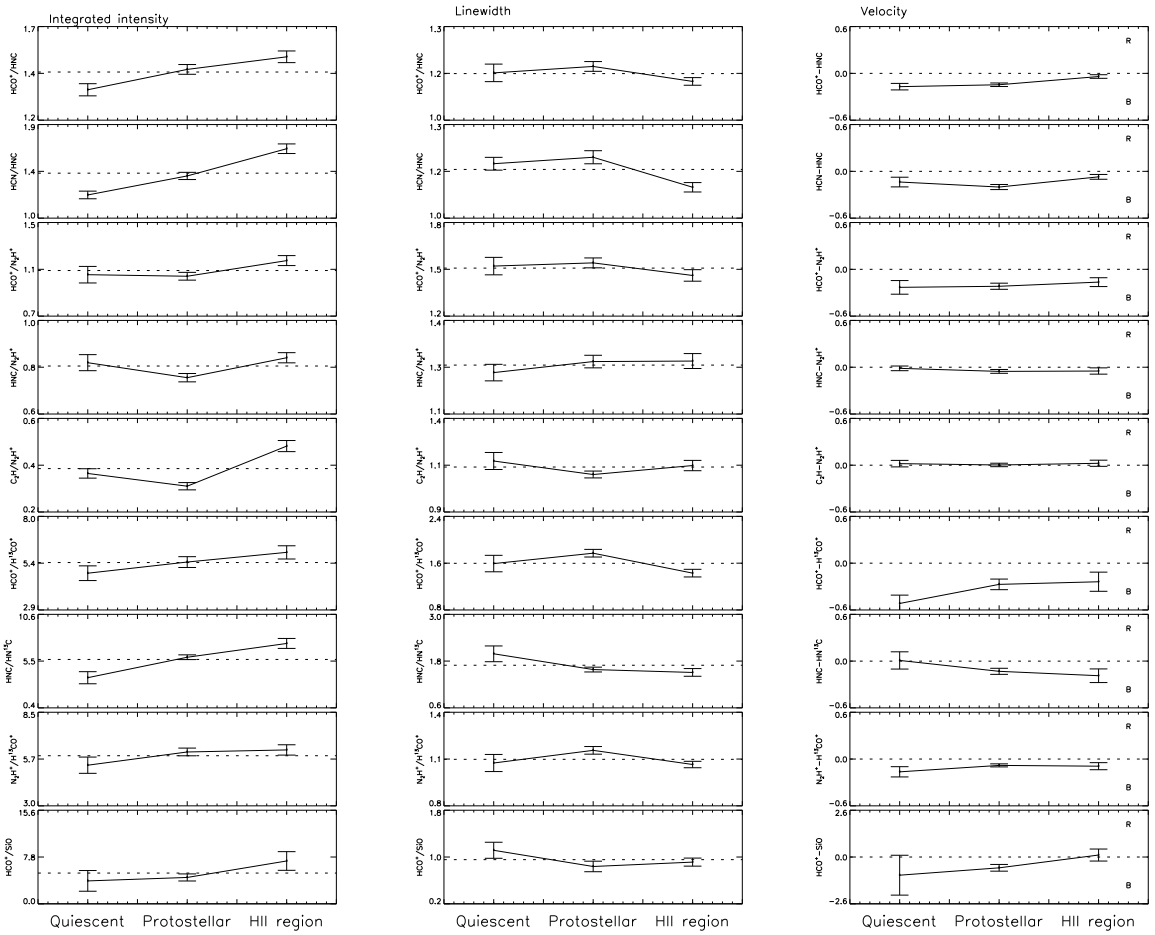

Figure 20. Trends as a function of IR-based category for clumps located outside of the CMZ (i.e., ± 10 degrees of the Galactic Centre). *Left column*: median in the distribution of the ratio of integrated intensities (the dotted lines mark the mean value of the plot range and are included to help identify trends). *Middle column*: median in the distribution of the ratio of derived linewidths (the dotted lines mark the mean value of the plot range and are included to help identify trends). *Right column*: median in the distribution of the velocity differences (the dotted lines mark the zero point, the plot ranges are symmetric about zero, and labels of 'R' and 'B' are included to indicate the direction of any red/blue asymmetries). In all plots the error bars show the uncertainty in the median value as calculated by bootstrap resampling with replacement (e.g., Simpson & Mayer-Hasselwander 1986).

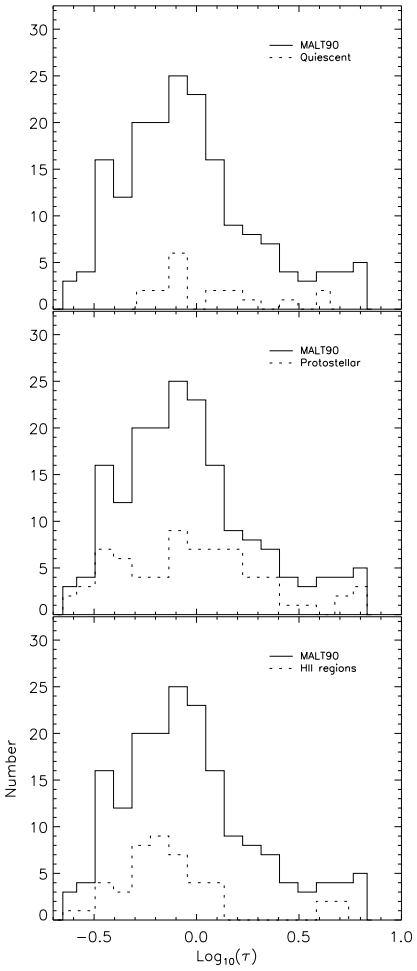

Figure 21. Histograms of the measured opacities for clumps located outside of the CMZ (i.e., ± 10 degrees of the Galactic Centre). In all panels the solid histogram shows the distribution derived from the full survey, while the dotted histograms show the distributions for each of the IR-based categories. We find that the distribution of τ from the full survey has a median value of ∼0.8. The differences in the overall distributions for the quiescent clumps and H II regions indicates a trend of decreasing opacity with increasing evolutionary stage.